EMERGING MATERIALS FOR PHYSICALLY RECONFIGURABLE ANTENNA TECHNOLOGIES

A Thesis

by

DAVID THOMAS GRAYSON

Submitted to the Office of Graduate and Professional Studies of
Texas A&M University
in partial fulfillment of the requirements for the degree of

MASTER OF SCIENCE

Chair of Committee,	Gregory H. Huff
Committee Members,	Robert D. Nevels
	Jean-Francois Chamberland
	Richard J. Malak
Head of Department,	Miroslav M. Begovic

August 2017

Major Subject: Electrical Engineering

ABSTRACT

The goal of this work is to demonstrate the fabrication and operation of reconfigurable microwave devices that incorporate emerging materials such as liquid metals and dielectric fluids, in order to foster a more effective collaboration between the material science and microwave engineering communities. This goal is accomplished by outlining the design, fabrication, and measurement processes of a few prototype devices. The first device is a series stub-based microwave band-stop filter that uses dielectric fluids in a 3D-printed channel to change the effective length of the filter stubs to enable frequency reconfigurability. A method for using the reconfigurable properties of the filter to determine the dielectric constant of the fluid is also developed and evaluated. The same band-stop filter design is modified by replacing the fixed copper stubs with an acrylic channel filled with eutectic gallium indium (EGaIn) to allow the physical length of the stubs to change dynamically as a mechanism for frequency reconfigurability. Another device presented in this work is a stretchable microstrip patch antenna made from silver thermoplastic polyurethane (AgTPU) printed on spandex. Stretching the spandex material changes the physical length of the patch to reconfigure the operating frequency. A simulation of the antenna shows that stretching only the half of the antenna with the feedline results in a better impedance match compared to when stretching the whole antenna. The last device presented is a patch antenna with a flexible, integrated pumping mechanism that can be used to drive fluid networks that enable frequency reconfigurability.

CONTRIBUTORS AND FUNDING SOURCES

This work was supported by a thesis committee consisting of Professor Gregory Huff (committee chair), Professor Robert Nevels, and Professor Jean-Francois Chamberland of the Department of Electrical and Computer Engineering, and Professor Richard Malak of the Department of Mechanical Engineering.

Fellow Texas A&M student Hong Pan was consulted for advice on the design of the liquid metal channel for the filter discussed in Chapter 5. The spandex layer of the printed metal patch antenna discussed in Chapter 6 was provided by Dr. Giorgio Bazzan of the Air Force Research Laboratory. All other work conducted for the thesis was completed by the student independently.

Funding for this work was made possible in part by the U.S. Air Force under Contract FA8650-11-D-5800, Task Order 0012, Subcontract 15-S7412-08-C1.

NOMENCLATURE

CPW	Coplanar Waveguide
ε_r	Relative Permittivity or Dielectric Constant
ε_{eff}	Effective Dielectric Constant
λ_{eff}	Effective Wavelength
EGaIn	Eutectic Gallium Indium
AgTPU	Silver Thermoplastic Polyurethane
AFRL	Air Force Research Lab

TABLE OF CONTENTS

Page

Page

LIST OF FIGURES

Page

Page

Page

LIST OF TABLES

Page

CHAPTER I

INTRODUCTION

The current collaborative efforts of the material science and microwave engineering communities are creating numerous opportunities to advance the capabilities of microwave systems. Materials such as liquid metals and dielectric fluids are finding new applications in the realm of physically reconfigurable microwave devices and antennas [1-4]. However, there are challenges in the development of these devices due to the different fabrication techniques needed to integrate fluids and other materials into typical microwave designs. While many devices developed in recent years have overcome these challenges, there still exists a need to refine the fabrication and measurement processes of microwave devices that use new materials in order to facilitate the development of future reconfigurable devices. This thesis is focused on encouraging a closer collaboration between the material science and microwave engineering communities by presenting the design, fabrication, and measurement of a few reconfigurable microwave devices that incorporate liquid metals, dielectric fluids, and other materials finding new uses in microwave systems.

One of the devices discussed in this thesis is a band-stop filter that uses dielectric fluids to shift the frequency of the stop-band region. As an additional experiment, a method for using the filter response to determine the dielectric constant of the dielectric fluid is developed and evaluated. This experiment shows how the reconfigurable filter can be used as a fluid sensor by measuring the frequency response of the filter with

different dielectric fluids. Another band-stop filter design is presented that uses a liquid metal alloy, eutectic gallium indium (EGaIn), as a movable conductor to change the physical design of the filter and enable frequency reconfigurability. Another reconfigurable device discussed in this thesis is a stretchable microstrip patch antenna that is made from a liquid conductor, silver thermoplastic polyurethane (AgTPU), printed on spandex. A different patch antenna concept is also presented that integrates a flexible pumping mechanism to control the fluid networks for reconfigurable devices.

The devices discussed in this thesis comprise only a small sample of the many possible reconfigurable devices that utilize new materials. Many of the devices presented involve the use of additive manufacturing techniques, such as 3D printing, to fabricate fluid channels and supporting structures. The fabrication and measurement processes discussed in this work will help the material science and microwave engineering communities gain a better understanding of the challenges involved in the collaborative design process of these new devices and the possible solutions to overcome these challenges to advance the capabilities of microwave systems.

CHAPTER II

BACKGROUND

Coplanar Waveguide

Two of the devices presented in this thesis use a coplanar waveguide (CPW) transmission line. CPW is a planar transmission line structure that consists of a center conductor surrounded by a ground plane on either side, as shown in Figure 1.

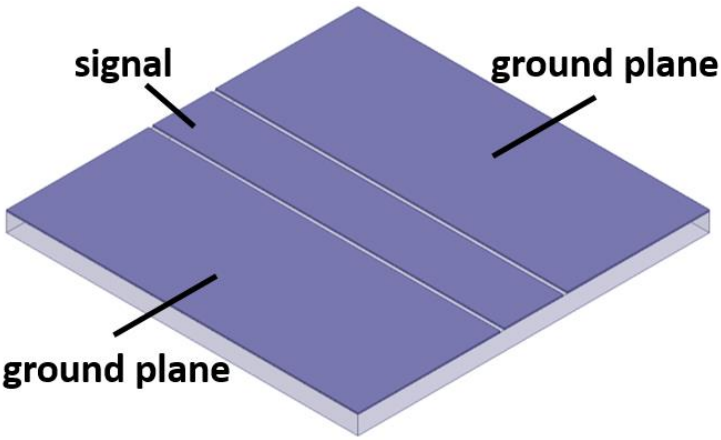

Figure 1. Coplanar Waveguide Transmission Line Structure

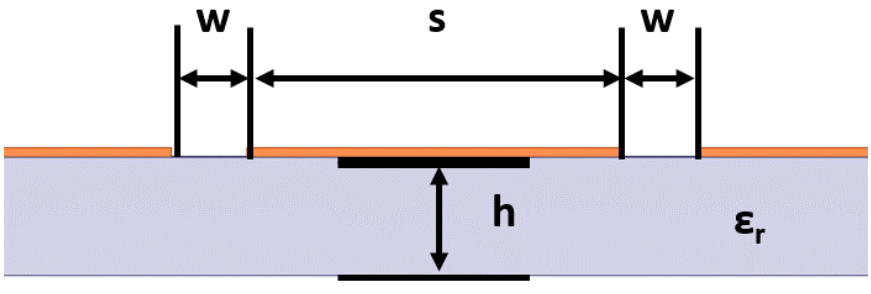

Figure 2. Cross Section Diagram of Coplanar Waveguide Transmission Line

These conducting planes are on the top layer of a substrate such as FR-4. Figure 2 shows a diagram of the cross section of a CPW line with the relevant dimensions labeled. The characteristic impedance of the line is a function of the signal line width, s, the gap width, w, between the signal line and ground plane, the height of the substrate, h, and the substrate dielectric constant, ε_r. The exact calculation of the characteristic impedance is rather complex and beyond the scope of this discussion. More information on the characteristic impedance of CPW transmission lines can be found in [5]. The 50 ohm CPW line used for the devices presented in this thesis is designed by fixing the signal line width, substrate height, and substrate dielectric constant to common values for a 62 mil FR-4 substrate and then conducting simulations using ANSYS HFSS with different values of the gap width until the characteristic impedance was approximately equal to 50 ohms. The dimensions of this 50 ohm CPW line are summarized in Table 1.

Dimension Name	Value
s	5.000 mm
h	1.575 mm
w	0.381 mm

Table 1. Relevant Dimensions of 50 Ohm Transmission Line

For a CPW line with a substrate on bottom and air on top, the effective dielectric constant, ε_{eff}, of the transmission line is approximated according to Equation (2.1) as a function of the dielectric constant of the substrate on bottom, ε_r, and the dielectric constant of the air above, which is equal to 1 [5].

$$\varepsilon_{eff} \approx \frac{1+\varepsilon_r}{2} \quad (2.1)\ [5]$$

The CPW line used in the devices in this thesis is made on an FR-4 substrate, which has a dielectric constant of $\varepsilon_r = 4.4$. According to Equation (2.1), the effective dielectric constant of this CPW line is approximately $\varepsilon_{eff} = 2.7$.

Microstrip Patch Antenna

This thesis presents two reconfigurable antenna designs based on the common microstrip patch antenna. The basic edge-fed patch antenna design consists of a rectangular conductive patch on a substrate over a ground plane, with a microstrip feedline connected to one of the edges of the patch, as shown in Figure 3.

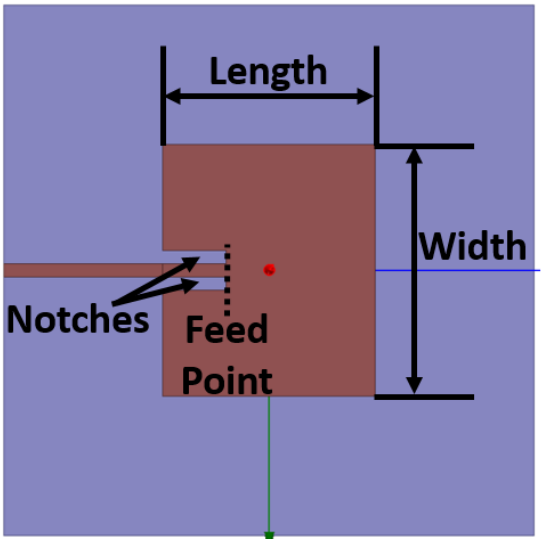

Figure 3. Diagram of Edge-Fed Patch Antenna

The design process of the patch antenna consists of a few equations to calculate the length and width of the patch for a given substrate and operating frequency. This design process is discussed in detail in [6]. For the purpose of this thesis, the main aspect of the design is that the length of the patch is slightly less than a half-wavelength at the operating frequency [6].

An inset feed is created by cutting out two notches on either side of the feedline as shown in Figure 3. The location of the inset feed point effects the resonant input impedance of the patch antenna, with a higher impedance at the edge of the patch and a lower impedance at the center of the patch [6]. Figure 4 shows how the antenna can be impedance matched to the feedline by changing the location of the feed point. The impedance traces on the Smith chart in Figure 4(a) correspond to the feed point locations of the same color in Figure 4(b).

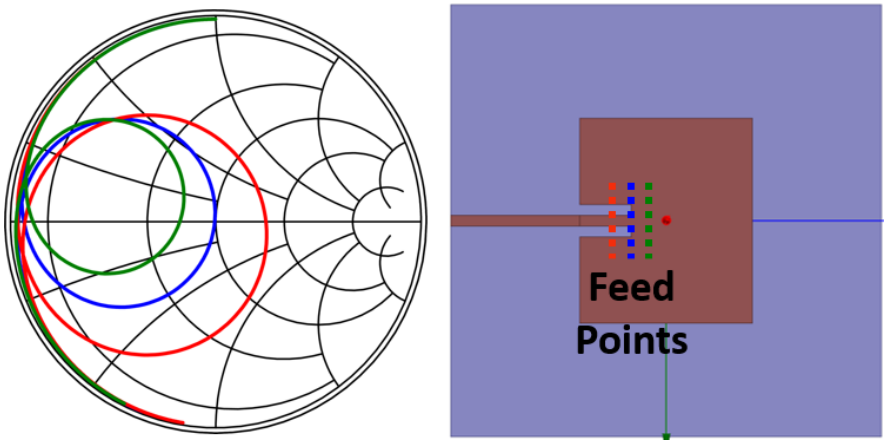

(a) (b)

Figure 4. (a) Smith Chart Curves for Patch Antenna with Different Feed Points
(b) Diagram of Feed Point Locations

An impedance match is indicated by a trace crossing the center of the Smith chart. The shape of the green trace on the Smith chart indicates that the input impedance is too low, and this corresponds to a feed point closer to the center of the patch. The red trace on the Smith chart indicates a higher input impedance than desired, corresponding to a feed point that is too close to the edge of the patch. The blue trace on the Smith chart crosses the center of the Smith chart, indicating a good impedance match. This shows how the feed point for a good impedance match can be found by moving the feed point closer to the center or closer to the edge of the patch depending on the Smith chart data. This technique is used in the design of the patch antennas presented in this thesis to obtain precise impedance matches in simulation before fabricating a prototype.

Scattering Parameters

The analysis of the reconfigurable filters presented in this thesis relies mainly on the measurement of the scattering parameters, or S-parameters, of the filter. The S-parameters are related to the incident and reflected voltage waves on the ports of an N-port network, and they can be measured directly with a network analyzer [7]. Figure 5 depicts the voltage waves in a 2-port network, such as a filter.

Figure 5. Diagram of a 2-Port Network

In this diagram, a_1 and b_1 are the incident and reflected voltage waves at port 1, respectively, and a_2 and b_2 are the incident and reflected voltage waves at port 2, respectively. The relation of the S-parameters to the incident and reflected voltage waves is expressed in Equation (2.2) and Equation (2.3).

$$b_1 = S_{11}a_1 + S_{12}a_2 \quad (2.2)\ [8]$$

$$b_2 = S_{21}a_1 + S_{22}a_2 \quad (2.3)\ [8]$$

The main S-parameter that is discussed in this thesis is S_{21}, which is the ratio of the output voltage wave at port 2 to the input voltage wave at port 1, in the absence of an input at port 2. This essentially describes the transmission of a voltage wave from port 1 to port 2. The magnitude of S_{21} is typically expressed in dB as a measure of the loss or gain through a 2-port device. The measurement of S_{21} over a frequency range is used to characterize devices such as the microwave filters discussed in this thesis.

CHAPTER III

H-SLOT COPLANAR WAVEGUIDE FILTER

Design Overview

The H-slot coplanar waveguide (CPW) filter is designed to serve as a demonstration vehicle for multiple experiments in frequency reconfigurable microwave devices with various materials. The goal of this design is to have a relatively narrow frequency response that is highly dependent on a single physical parameter that can easily be modified. Thus, the device can be made frequency reconfigurable by altering the physical parameter that most contributes to the change in the frequency response. The filter design, shown in Figure 6, consists of an "H-shaped" slot cut out of a 50 ohm CPW transmission line, which results in two equal length series stubs separated by a gap. This design is inspired by existing series-stub CPW band-pass filter designs, with modifications to produce band-stop characteristics [9, 10].

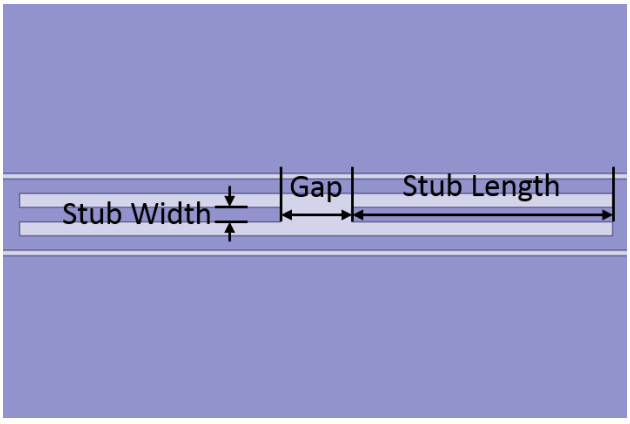

Figure 6. Diagram of H-Slot Filter (Top View)

The filter is fabricated on an FR-4 substrate with a thickness of 62 mil and a dielectric constant of $\varepsilon_r = 4.4$, as shown in Figure 7. The relevant dimensions of the fabricated filter are summarized in Table 2 using the dimension names established in Figure 6. The device is designed to act as a band-stop filter with a center frequency of 2.4 GHz. The two series stubs are approximately a quarter-wavelength at the center frequency. The filter is simulated using ANSYS HFSS, and the simulated and measured S_{21} magnitude data is compared in Figure 8.

Figure 7. H-Slot Filter Fabricated on 62 mil FR-4 ($\varepsilon_r = 4.4$)

Dimension Name	Value
Stub Length	18.5 mm
Stub Width	1.0 mm
Gap	1.0 mm

Table 2. Relevant Dimensions of Fabricated H-Slot Filter on FR-4

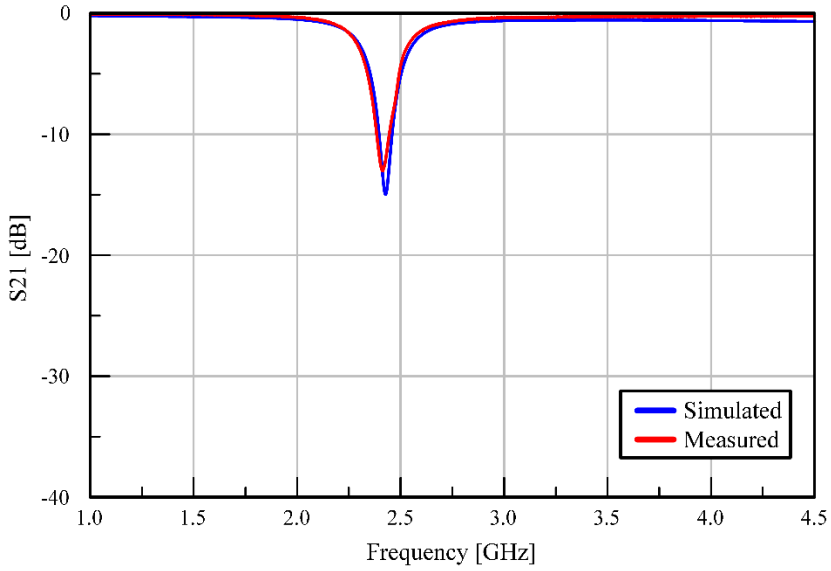

Figure 8. S_{21} Magnitude [dB] of Simulated and Measured H-Slot Filter

The shape of the S_{21} curves in Figure 8 shows that this filter exhibits characteristics of a band-stop filter. The frequency of the minimum S_{21} magnitude, or center frequency, of the fabricated filter is 2.413 GHz while the center frequency of the simulated filter is similar at 2.427 GHz. The S_{21} magnitude at the center frequency for the fabricated filter is -13.063 dB, which is almost 2 dB higher than that of the simulated filter at -14.968 dB. These discrepancies between measured and simulated data are within acceptable limits for the purpose of this study, which is mainly concerned with demonstrating frequency reconfigurability techniques using this device.

Parameter Variation

As previously stated, the frequency response of the filter, particularly the center frequency, should ideally be dependent on a single physical parameter for the purpose of

this study. If the filter response depends heavily on multiple design parameters, then the mechanisms to enable frequency reconfigurability may be more complex and difficult to implement. A series of HFSS simulations are presented in order to examine the dependence of the frequency response on the key physical design parameters: gap, stub width, and stub length.

The first simulation varies the size of the gap between the two stubs from 0.5 mm to 7.5 mm, while keeping the stub width and stub length constant at the values listed in Table 2. Figure 9 shows the S_{21} magnitude response of the filter for the various gap sizes.

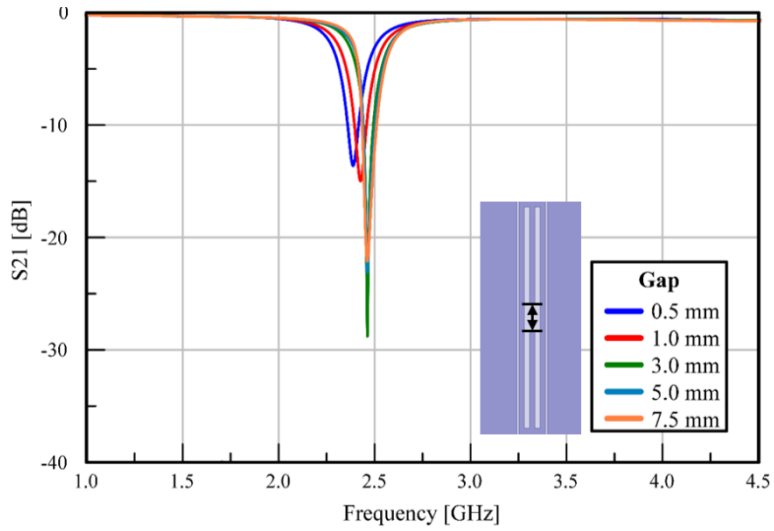

Figure 9. S_{21} Magnitude [dB] of H-slot Filter for Various Gap Sizes

The center frequency of the filter increases slightly from 2.389 GHz to 2.462 GHz as the gap size increases from 0.5 mm to 7.5 mm. It is worth mentioning that the magnitude of S_{21} at the center frequency decreases as the gap size increases up to 3.0

mm, at which point it begins to increase as the gap size increases from 3.0 mm to 7.5 mm. This is possibly due to the interaction of effective inductance and capacitance in the gap, stubs, and the rest of the center part of the CPW line. The development and analysis of an equivalent circuit model of this device, however, is beyond the scope of this study. Since the center frequency of the filter no longer shifts as the gap size increases beyond 3.0 mm, this parameter is not considered to have the most impact on the center frequency that can be utilized for significant frequency reconfigurability.

The next simulation varies the stub width from 0.25 mm to 2.5 mm, while keeping all other parameters constant at the values listed in Table 2. The magnitude of S_{21} for the various stub widths is show in Figure 10.

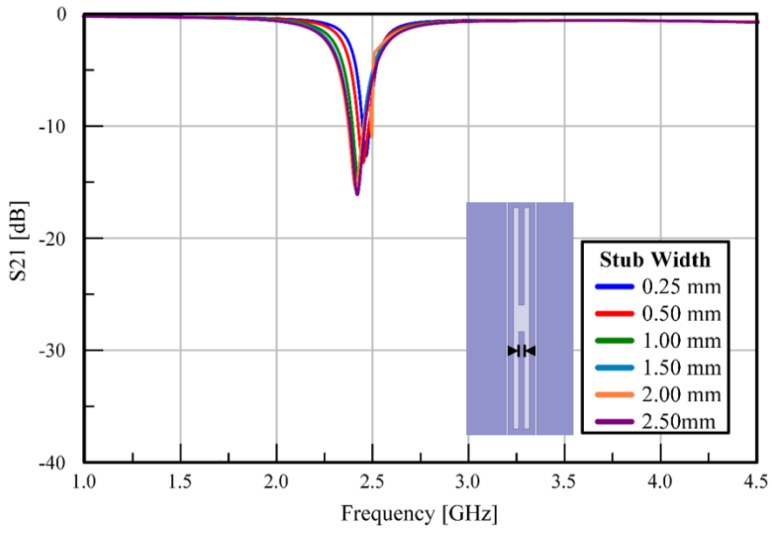

Figure 10. S_{21} Magnitude [dB] of H-slot Filter for Various Stub Widths

As with the gap size, the stub width does not have a large impact on the center frequency of the filter. The center frequency decreases from 2.466 GHz to 2.421 GHz as

the stub width increases from 0.25 mm to 2.50 mm. This is only about a 1.8% frequency shift when the stub width is increased by a factor of 10, which is not enough to be used for significant frequency reconfigurability. Additionally, the stub width is constrained by the width of the 50 ohm CPW line, limiting the minimum center frequency that could be achieved.

The final simulation performed varies the stub length from 14.0 mm to 20.0 mm, while keeping the other parameters constant at the values listed in Table 2. Figure 11 shows the frequency response of the filter for the various stub lengths.

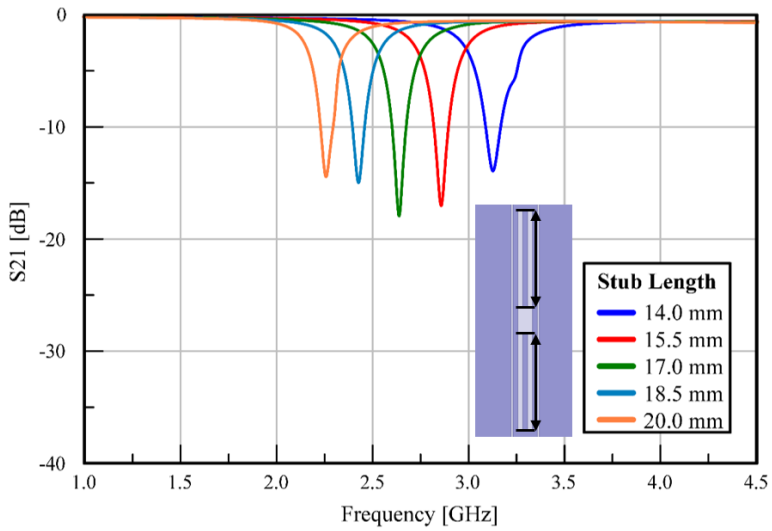

Figure 11. S_{21} Magnitude [dB] of H-slot Filter for Various Stub Lengths

As the stub length increases from 14.0 mm to 20.0 mm, the center frequency of the filter decreases from 3.126 GHz to 2.258 GHz. This is about a 27.8% shift in the center frequency, while the stub length only increases by a factor of 1.43. The magnitude of S_{21} at each center frequency varies between approximately -14 dB and -18 dB. This is

acceptable for the purpose of this study, as the S_{21} curves in Figure 11 show frequency responses with easily distinguishable center frequencies that depend mainly on a single parameter, the stub length.

Upon further examination, the stub length is approximately a quarter-wavelength at the center frequency. The effective wavelength, λ_{eff}, for a given frequency, f, can be calculated using Equation (3.1), where c is the speed of light in free space and ε_{eff} is the effective dielectric constant of the medium.

$$\lambda_{eff} = \frac{c}{f\sqrt{\varepsilon_{eff}}} \tag{3.1}$$

The effective dielectric constant of the CPW line is $\varepsilon_{eff} = 2.7$, from Equation (2.1). Table 3 shows the value of a quarter-wavelength at each center frequency shown in Figure 11 compared to the corresponding stub length.

Center Frequency	$\lambda_{eff}/4$	Stub Length	% Difference
3.126 GHz	14.6 mm	14.0 mm	4.2 %
2.857 GHz	16.0 mm	15.5 mm	3.0 %
2.638 GHz	17.3 mm	17.0 mm	1.8 %
2.427 GHz	18.8 mm	18.5 mm	1.6 %
2.258 GHz	20.2 mm	20.0 mm	1.1 %

Table 3. Comparison of Stub Length to $\lambda_{eff}/4$ at Center Frequency

This insight makes the filter response more predictable and simplifies the design process. This also suggests that the filter design can be easily scaled to operate at

different frequencies or to be fabricated on different substrates. Frequency reconfigurability of the H-slot filter can be achieved by implementing a mechanism to alter the effective length of the stubs. Two such mechanisms, one using dielectric fluid and the other using liquid metal, will be discussed in the following chapters.

CHAPTER IV

DIELECTRIC FLUID RECONFIGURABILITY OF H-SLOT FILTER

Design Overview

As mentioned in the previous chapter, the H-slot filter can be made frequency reconfigurable by altering the effective length of the two stubs. One way to do this is to alter the effective dielectric constant of the transmission line. In the case of CPW, the effective dielectric constant is a function of the dielectric constant of the surrounding materials. For the fabricated H-slot filter in Chapter 3, the CPW line is surrounded by FR-4 ($\varepsilon_r = 4.4$) on the bottom and air ($\varepsilon_r = 1$) on the top. Introducing other dielectric materials near the transmission line will change the effective dielectric constant of the medium. From Equation (3.1), an increase in the effective dielectric constant results in a decreased effective wavelength at a particular frequency. Since the length of the stubs is held constant, the frequency at which the stubs equal a quarter-wavelength is decreased. Chapter 3 demonstrated that the center frequency of the filter is the frequency at which the stubs are approximately a quarter-wavelength. This chapter presents the results of an experiment in which a fluid channel is placed directly over the H-slot filter and fluids with varying dielectric constants flow through the channel in order to change the effective dielectric constant, and thus the center frequency, of the filter.

A goal of this thesis is to incorporate additive manufacturing techniques into reconfigurable microwave devices. To help achieve this goal, the fluid channel for this filter is 3D-printed from a commonly used polylactic acid (PLA) material. Figure 12

shows a diagram of the fluid channel on the H-slot filter and its relevant dimensions, which are summarized in Table 4.

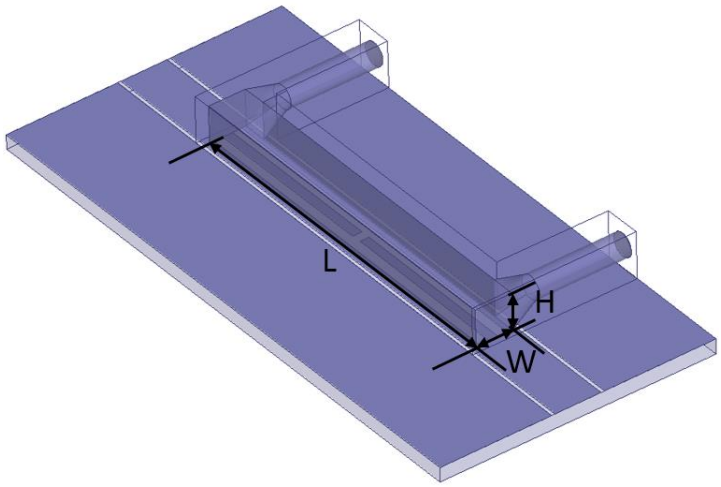

Figure 12. Diagram of Fluid Channel Attached to H-Slot Filter

Dimension Name	Value
L	38.0 mm
W	4.0 mm
H	4.0 mm

Table 4. Relevant Dimensions of 3D-Printed Fluid Channel

The fluid channel is open on the bottom in the region that covers the H-slot such that the fluid occupies the space directly above the slot in order to have a relatively large influence on the effective dielectric constant. The channel is secured in place on top of the H-slot filter and sealed using epoxy as shown in Figure 13. Two syringe tips are

attached to either side of the channel and sealed with epoxy as well to provide easy access to insert the fluid.

Figure 13. Fabricated H-Slot Filter with 3D-Printed Fluid Channel

Dielectric Fluid Selection

This experiment requires a set of fluids that comprise a variety of dielectric constants in order to demonstrate the frequency reconfigurability of this filter. The dielectric constant of each fluid needs to be relatively constant over the measured frequency range for this experiment, which is 1.0 GHz to 4.5 GHz. To simplify the fluid selection process, only fluids that are readily found in the lab are considered. An Agilent 85070E Dielectric Probe Kit is used to measure the dielectric constant of readily available fluids to determine eligibility for this experiment and the results are shown in Figure 14.

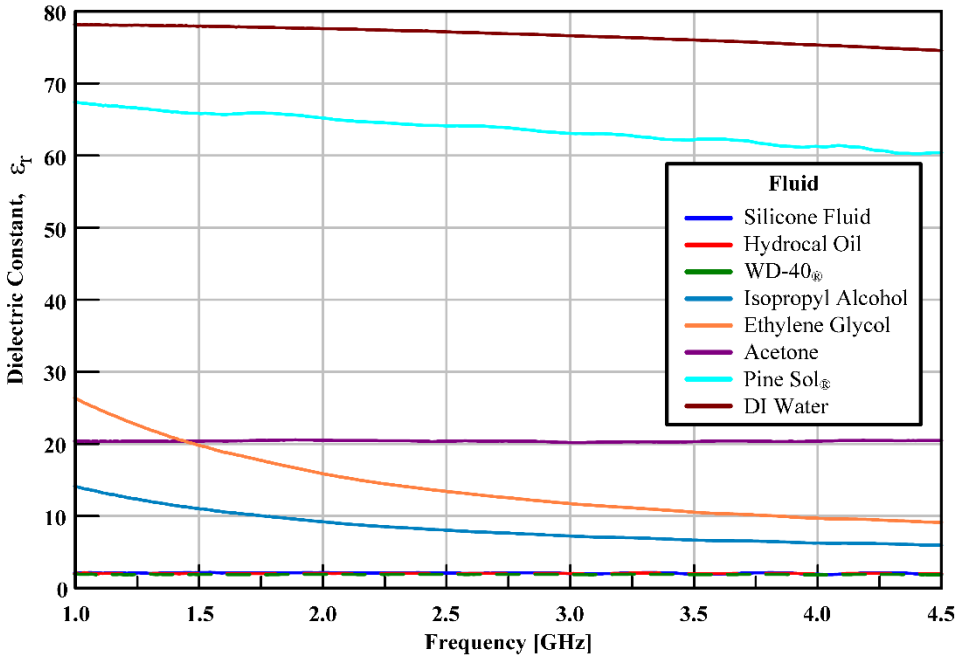

Figure 14. Measured Dielectric Constants of Fluid Candidates

According to the results in Figure 14, isopropyl alcohol, ethylene glycol, Pine Sol®, and deionized (DI) water are not considered eligible fluids for this experiment because their dielectric constants vary too much over the measured frequency range. In addition, the remaining fluid candidates' dielectric constants are not diverse enough to demonstrate reconfigurability over several center frequencies. However, acetone and WD-40® are observed to combine into a somewhat homogeneous mixture for a few minutes before gradually separating into distinct liquids. In order to expand the variety of dielectric constants available for the experiment, individual mixtures of acetone and WD-40® with varying concentrations were measured and the results are shown in Figure 15. The concentrations are labeled as percent of acetone in WD-40® by volume, and

each mixture is a total of 50 mL. For example, the “20% Acetone” mixture contains 10 mL of acetone and 40 mL of WD-40®.

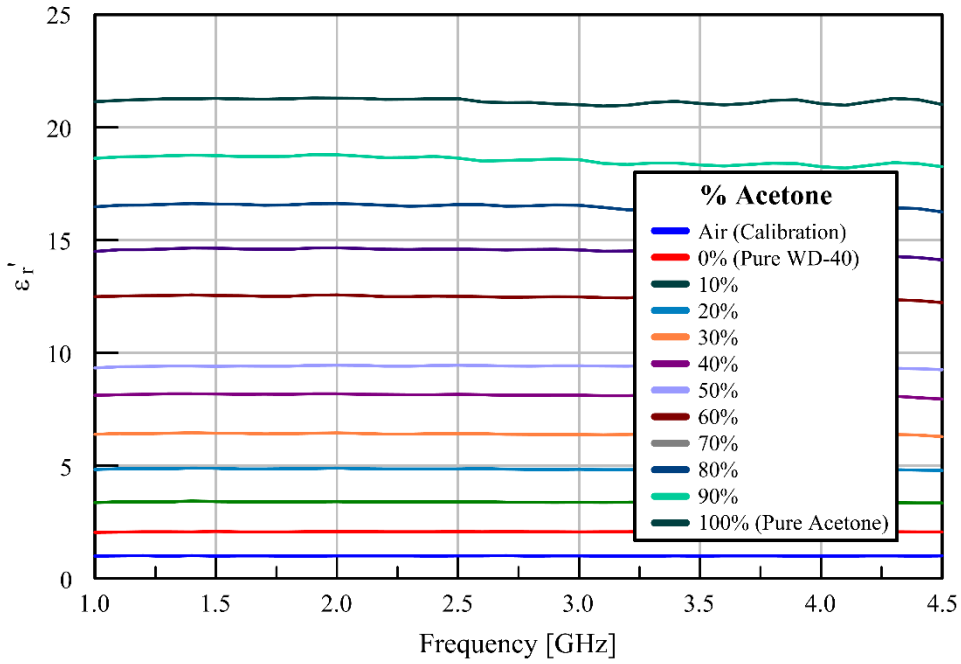

Figure 15. Measured Dielectric Constants of 50 mL Acetone/WD-40® Mixtures

The mixtures are shown to have a dielectric constant somewhere in between that of acetone and WD-40® if measured within a few minutes of combining, and the dielectric constant monotonically increases with increasing concentration of acetone. The results in Figure 15 show that the acetone and WD-40® mixtures yield the variety of dielectric constants desired for the frequency reconfigurability experiment. Using these mixtures, the dielectric constant of the fluid in the channel can be controlled within a range of approximately 2 to 21. In addition, each mixture’s dielectric constant is distinct and relatively constant in the measured frequency range.

Methodology

For this frequency reconfigurability experiment, the H-slot filter is connected to a calibrated Agilent network analyzer measuring the S_{21} magnitude response. The S_{21} response is recorded for the filter with only air in the channel. This measurement is used in later steps as a reference to determine when the filter channel is clean. The dielectric probe kit is calibrated using three measurement standards: air, DI water, and a short circuit device that comes with the kit. The tip of the probe is cleaned with acetone and dried. After allowing time to dry, the probe kit is validated by measuring the dielectric constant of the air until it gives the correct result of approximately "1" across all frequencies. This ensures that the acetone used to clean the probe does not affect the measurement.

The first fluid is prepared by pouring 50 mL of WD-40® into a beaker. The average dielectric constant of the fluid across the frequency range is measured by inserting the probe into the liquid and recording the value from the software interface. 5 mL of the fluid is inserted into the fluid channel with a syringe and the S_{21} magnitude response is recorded on the network analyzer while the fluid is held in place in the channel.

The fluid channel is then rinsed with isopropyl alcohol and connected to an air compressor to dry. While the channel is drying, the probe is cleaned with acetone and validated by measuring the air as previously described. After approximately 5 minutes of drying with the air compressor, the filter is connected to the network analyzer to measure the S_{21} response with only air in the channel. This measurement is repeated until it

agrees with the original measurement with only air in the channel, and additional drying time is given if necessary.

The next fluid, comprised of 10% acetone and 90% WD-40®, is prepared by combining 5 mL of acetone and 45 mL of WD-40® in a beaker and stirring well. The average dielectric constant of the fluid is measured as previously described, and the rest of the steps are repeated to obtain the S_{21} magnitude response with this fluid and to rinse and dry the channel. This sequence continues for each of the remaining fluids until there are S_{21} magnitude response measurements for each of the fluid mixtures presented in Figure 15.

Experimental Results

The measured S_{21} magnitude response curves from this experiment are presented in Figure 16. The curves are labeled according to the measured dielectric constant of the fluid used for each measurement. The frequency at which the S_{21} magnitude is at a minimum is referred to as the center frequency for this discussion. These results show that the center frequency decreases as the dielectric constant of the fluid increases. This is because the effective wavelength of the CPW line decreases as the effective dielectric constant increases, according to Equation (3.1). The filter stub lengths are held constant during this experiment, but the effective wavelength is changing. As the effective wavelength decreases, the stub lengths equal a quarter-wavelength at a lower frequency, in other words, where the wavelength is longer. This filter has been shown in the previous chapter to have a center frequency where the stub lengths are approximately

equal to a quarter-wavelength. Therefore, these results confirm the expectation that the center frequency decreases as the dielectric constant of the fluid increases.

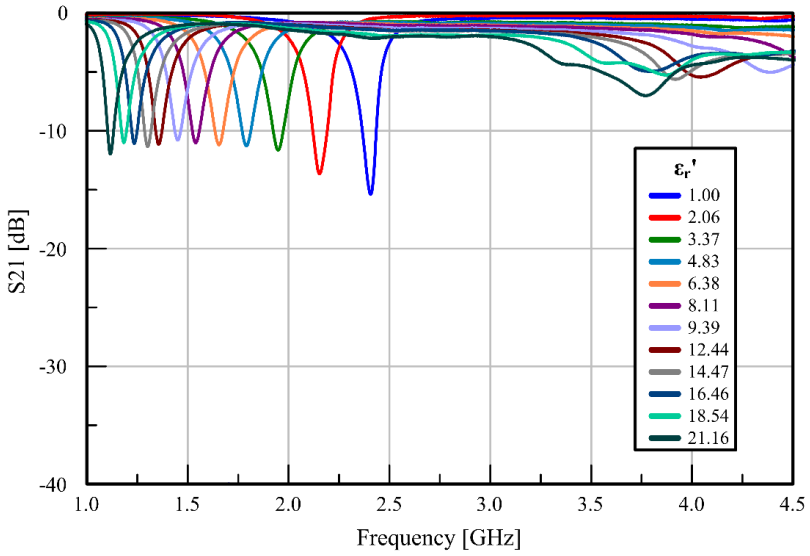

Figure 16. Measured S_{21} Magnitude for H-Slot Filter with Dielectric Fluid

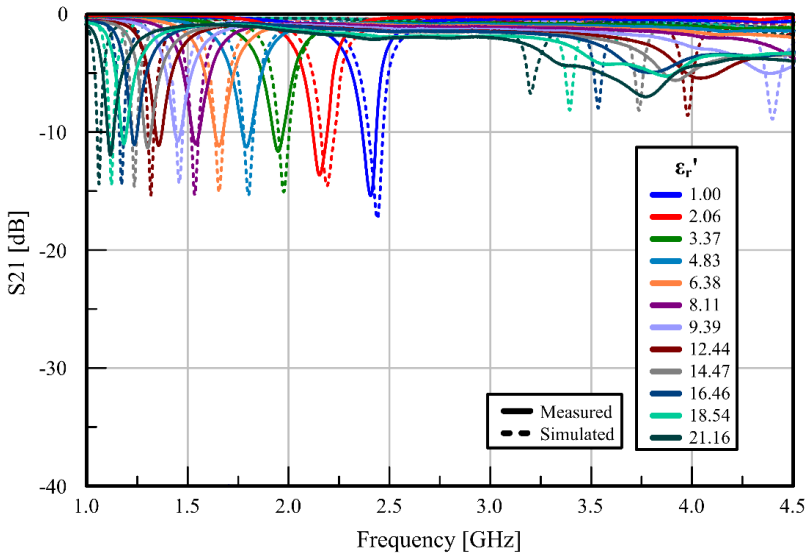

Figure 17. Measured and Simulated S_{21} Magnitude of H-Slot Filter with Dielectric Fluid

Figure 17 shows a comparison of the measured results of this experiment with a simulation of this experiment in HFSS. The fluid region in the simulation is modeled using the measured dielectric constant of each fluid used in the experiment in order to compare the results directly. The simulated results show center frequency shifts similar to the measured data. There are, however, some key differences such as the fact that the magnitude of S_{21} at the center frequency is lower in the simulation compared to the measured data. Also, the additional band-stop regions in the 3.0 GHz to 4.5 GHz range are more pronounced in the simulated data.

It is important to note that the simulated results in Figure 17 are obtained assuming a lossless fluid. In an attempt to bring the simulation into better agreement with the actual measured data, a new set of simulations were performed varying the loss tangent of the fluid, $\tan\delta$, from 0.0 to 0.1 while keeping the dielectric constant at $\varepsilon_r = 2.06$. The loss tangent is a material parameter used to quantify dielectric losses, with "0" being lossless and greater values corresponding to greater dielectric loss.

Figure 18 shows the simulated results of increasing the dielectric loss of the fluid. These results show that introducing loss in the simulation increases the magnitude of S_{21} at the center frequency and shifts the filter response to a slightly higher center frequency. The loss tangent of the fluids used in the experiment can be estimated by comparing these simulated results to the measured results. The simulation that uses a loss tangent of $\tan\delta = 0.02$ most closely reflects the measured data from the original experiment, so the loss tangent of the fluid is estimated to be $\tan\delta = 0.02$. Figure 19 shows the measured results of the original experiment, this time compared to a

simulation in which the fluid has a loss tangent of tanδ = 0.02. The results of this simulation are in better agreement with the measured results now that loss is incorporated into the model.

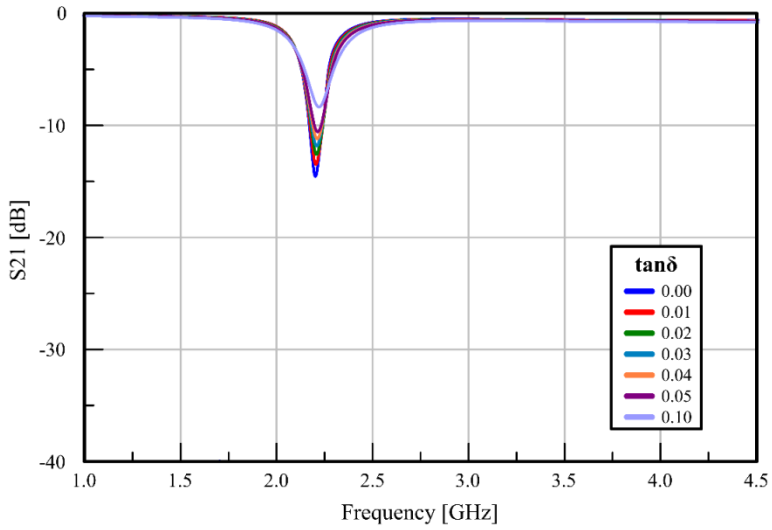

Figure 18. Simulated S_{21} Magnitude of H-Slot Filter with Lossy Fluid

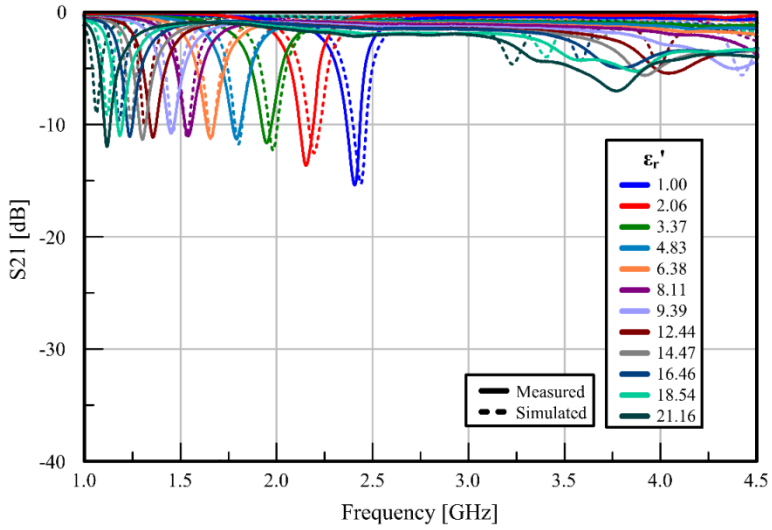

Figure 19. Measured and Simulated S_{21} Magnitude of H-Slot Filter using Dielectric Fluid with tanδ = 0.02

This simulation does not perfectly model the true characteristics of the fluids as it assumes that each fluid has the same loss tangent and that the loss tangent is constant over all frequencies. That is why there are still discrepancies between the measured and simulated data, especially for the fluids with the higher dielectric constants. Though the simulation has its flaws, it does support the measured observation that the center frequency decreases as the dielectric constant of the fluid increases. This experiment demonstrates just one of many ways in which 3D-printed parts enable the development of new frequency reconfigurable microwave devices.

Fluid Characterization

In the previous section, an experiment was presented that showed how the center frequency of the H-slot filter can be controlled by flowing different dielectric fluids through a channel over the slot. Since the center frequency of the filter is so closely related to the dielectric constant of the fluid, it is interesting to think of reversing the experiment by using the measured center frequency of the filter to determine the dielectric constant of the fluid. This would give the H-slot filter, and possibly other reconfigurable devices, the ability to act as a type of material measurement sensor in addition to being a microwave filter. This section outlines a method for developing an equation to predict the dielectric constant of a fluid based solely on the measured center frequency of the filter.

This technique utilizes the fact that the filter stub length is approximately equal to a quarter-wavelength at the center frequency of the filter. This is represented by

Equation (4.1), where l is the physical stub length, λ_{eff} is the effective wavelength, c is the speed of light in free space, f_c is the center frequency, and ε_{eff} is the effective dielectric constant of the medium.

$$l \approx \frac{\lambda_{eff}}{4} = \frac{c}{4f_c\sqrt{\varepsilon_{eff}}} \tag{4.1}$$

The effective dielectric constant can be approximated as a linear combination of two terms, ε_r and ε_{other}, as shown in Equation (4.2), where ε_r is the dielectric constant of the fluid, ε_{other} encapsulates the effective dielectric constant of all of the surrounding materials other than the fluid, and a_1 and a_2 are linear weighting factors.

$$\varepsilon_{eff} \approx a_1\varepsilon_r + a_2\varepsilon_{other} \tag{4.2}$$

This approximation is important because it allows Equation (4.1) to be rearranged to have ε_r isolated on one side of the equation, which is needed to be able to calculate the dielectric constant of the fluid from the other parameters. It is not unordinary to express the effective dielectric constant of a medium as the linear combination of multiple dielectric constants. Recall from Equation (2.1) that the effective dielectric constant for a typical CPW line is approximately equal to the arithmetic mean of the dielectric constant of the substrate below and that of the air above. In Equation (4.2), a_1 and a_2 are unknown weighting factors related to the electric

field distribution within the different materials, due to their geometrical arrangement around the CPW line. Since the only thing that changes in this experiment is the dielectric constant of the fluid, ε_r, it is not necessary to solve for a_1, a_2, or ε_{other} individually because they will be lumped together in a later step. The derivation continues by substituting Equation (4.2) into Equation (4.1), resulting in Equation (4.3).

$$l \approx \frac{c}{4f_c\sqrt{a_1\varepsilon_r + a_2\varepsilon_{other}}} \tag{4.3}$$

Next, Equation (4.4) is produced by rearranging Equation (4.3) to isolate ε_r on one side, with all other terms on the other side.

$$\varepsilon_r \approx \frac{c^2}{16a_1l^2f_c^2} - \frac{a_2\varepsilon_{other}}{a_1} \tag{4.4}$$

In this experiment, the only variables are ε_r and f_c, and all of the other terms remain constant. Therefore, Equation (4.4) can be simplified by combining all of the constants into just two constants, β_0 and β_1, and the resulting expression takes the form of Equation (4.5).

$$\varepsilon_r \approx \beta_0 + \beta_1 f_c^{-2} \tag{4.5}$$

Now that there is an equation that puts ε_r in terms of only f_c and constants, a least squares estimation method described in [11] is used to generate a best-fit curve for the measured data in the form of Equation (4.5). The measured data is used to form a system of equations, represented in matrix form in Equation (4.6).

$$y = X\beta \tag{4.6}$$

$$\text{where } y = \begin{bmatrix} \varepsilon_{r1} \\ \vdots \\ \varepsilon_{rN} \end{bmatrix}, X = \begin{bmatrix} 1 & f_{c1}^{-2} \\ \vdots & \vdots \\ 1 & f_{cN}^{-2} \end{bmatrix}, \text{ and } \beta = \begin{bmatrix} \beta_0 \\ \beta_1 \end{bmatrix}$$

Table 5 lists the measured dielectric constants and corresponding filter center frequencies from the experiment presented in the previous section.

Index	ε_r	f_c [GHz]
1	0.995	2.407
2	2.061	2.154
3	3.371	1.947
4	4.828	1.793
5	6.383	1.656
6	8.111	1.539
7	9.385	1.451
8	12.443	1.356
9	14.470	1.303
10	16.459	1.235
11	18.540	1.185
12	21.157	1.118

Table 5. Measured Fluid Dielectric Constants and H-Slot Filter Center Frequencies

The first dielectric constant value in Table 5 is less than one, which is theoretically impossible. This data was measured with the dielectric probe kit, which can exhibit some degree of measurement error. Even though this value is less than one, the best-fit curve that is developed from this data will not be affected much by this error since the magnitude of the error is relatively small.

The next step is to generate a best-fit equation from the measured data in the form of Equation (4.5). Equation (4.7) solves for the least squares estimator, $\hat{\beta}$, for this data set, as described in [11]. The solution to Equation (4.7) is given in Equation (4.8).

$$\hat{\beta} = (X^T X)^{-1} X^T y \tag{4.7} [11]$$

$$\hat{\beta} = \begin{bmatrix} \hat{\beta}_0 \\ \hat{\beta}_1 \end{bmatrix} = \begin{bmatrix} -5.3318 \\ 32.9715 \end{bmatrix} \tag{4.8}$$

Substituting the values for $\hat{\beta}_0$ and $\hat{\beta}_1$ into Equation (4.5) results in the best-fit expression shown in Equation (4.9).

$$\varepsilon_r \approx -5.3318 + 32.9715\, f_c^{-2} \tag{4.9}$$

Figure 20 shows the fluid dielectric constants from the experiment from the previous section and the corresponding measured and simulated center frequencies, along with the best-fit curve for the measured data from Equation (4.9).

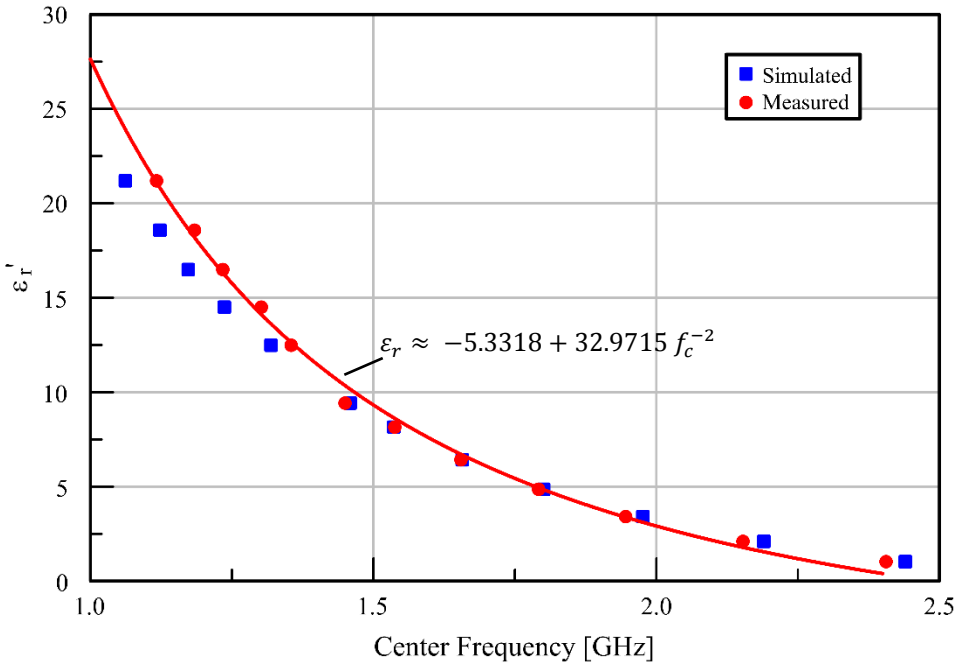

Figure 20. Fluid Dielectric Constants and Corresponding Filter Center Frequencies with Best-Fit Curve

The best-fit curve in Figure 20 fits most of the measured data quite well, but it is less accurate for dielectric constants near $\varepsilon_r = 1$ and $\varepsilon_r = 9$. The main issue with using Equation (4.9) for the best-fit curve is that it approaches a negative dielectric constant as the center frequency goes to infinity. However, practically speaking, the highest the center frequency will ever get is that for which the dielectric constant of the fluid is equal to one.

The results in Figure 20 suggest that this best-fit equation could be used to estimate the dielectric constant of a fluid given only the center frequency of the filter response. In order to verify this claim, five mixtures of random, unknown concentrations of Acetone and WD-40® are measured with the dielectric probe kit and then inserted into

the fluid channel while the S_{21} magnitude data is recorded, similar to the procedure described in Section 4.3. The channel is rinsed and dried between measurements and Equation (4.9) is used to predict the dielectric constant of the unknown fluid mixtures based solely on the measured center frequency of the filter. A measurement with only air in the channel is also recorded in order to test the accuracy of the equation with a very low dielectric constant. These predictions are compared to the dielectric probe measurements in Table 6.

Mixture Label	f_c [GHz]	$\varepsilon_{r,Predicted}$	$\varepsilon_{r,Measured}$	% Error
Air	2.372	0.528	0.999	47.090
1	1.633	7.032	6.623	6.178
2	1.896	3.840	3.630	5.777
3	2.168	1.683	1.849	8.970
4	2.039	2.599	2.640	1.578
5	1.251	15.736	17.444	9.790

Table 6. Measured and Predicted Dielectric Constant of Fluids in H-Slot Filter

The best-fit equation developed in this section can be used to predict the dielectric constant of fluids with around 1% to 10% error for most of the cases tested. The largest error occurred with only air in the channel, but this is expected based on the large difference between the measured data and the best-fit curve at dielectric constants very close to $\varepsilon_r = 1$ shown in Figure 20. More rigorous testing is required to validate this method for estimating the dielectric constant of materials. However, this experiment successfully demonstrates the possibility of using the H-slot filter as a type of material measurement sensor.

CHAPTER V

LIQUID METAL RECONFIGURABILITY OF H-SLOT FILTER

Design Overview

In Chapter 4, the H-slot filter was made frequency reconfigurable by changing the effective dielectric constant of the medium, and thus *effectively* changing the length of the filter stubs relative to the wavelength at a given frequency. This chapter discusses a different mechanism for enabling frequency reconfigurability for the filter, by *physically* changing the length of the stubs in order to tune the center frequency of the filter. This is accomplished by using a liquid metal alloy called eutectic gallium indium (EGaIn) in a new channel over the slot to replace the fixed-length stubs of the H-slot filter. The liquid metal stubs flow through the channel to change the stub length and thus, the center frequency of the filter. EGaIn is used in a variety of engineering applications, often as a non-toxic substitute for mercury. It is incorporated into the following experiment in order to demonstrate just one of many ways this popular material can be used to enable reconfigurable microwave devices.

This experiment requires a new channel design for the EGaIn to flow through to form the stubs. The new channel is made using a circuit-milling machine to cut a thin line, approximately 0.5 mm deep and 0.5 mm wide, into a small piece of 1/16-inch (≈1.6 mm) acrylic. The channel is open on the bottom side to allow contact with the CPW line. Two holes are drilled through the acrylic piece at either end of the channel to provide access points for the syringe injecting the EGaIn. Cylindrical regions on either side of

the channel are also cut out in order to provide an area for improved electrical contact between the EGaIn and the copper of the CPW line. Figure 21(a) and (b) show diagrams of the channel design with the relevant dimensions labeled. These dimensions are summarized in Table 7.

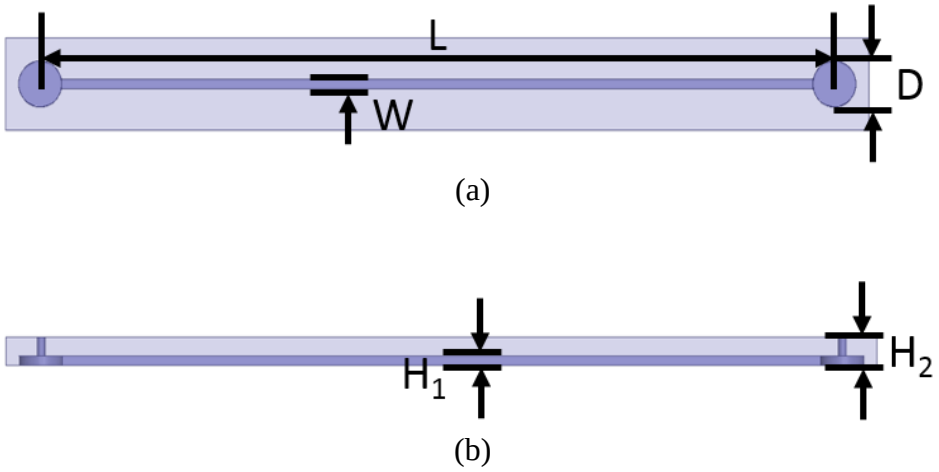

Figure 21. Diagrams of EGaIn Channel (a) Bottom View and (b) Side View

Dimension Name	Value
L	46.0 mm
D	2.5 mm
W	0.5 mm
H_1	0.5 mm
H_2	1.6 mm

Table 7. Relevant Dimensions of EGaIn Channel

The channel is placed over the rectangular slot such that the EGaIn flows directly across the slot to form the stubs for the H-slot filter, as shown in the simulation model in Figure 22.

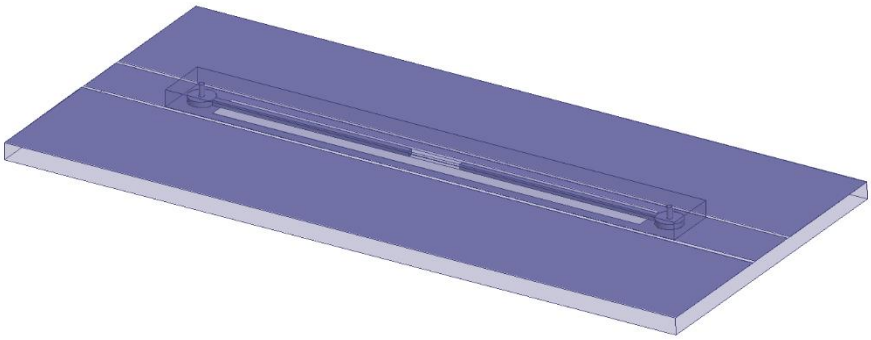

Figure 22. Simulation Model of H-Slot Filter with EGaIn Channel

The fabricated channel is attached to the CPW line and sealed using epoxy. A very thin string is used to “floss” the channel and keep it clear of the epoxy while it sets. Figure 23 shows the fabricated filter, which consists of the CPW line with a rectangular slot and the attached channel for the EGaIn filter stubs. The fabricated channel in Figure 23 includes seven additional holes spaced 5 mm apart, which allow the EGaIn stubs to be positioned more precisely. The use of these holes is explained in more detail in the next section.

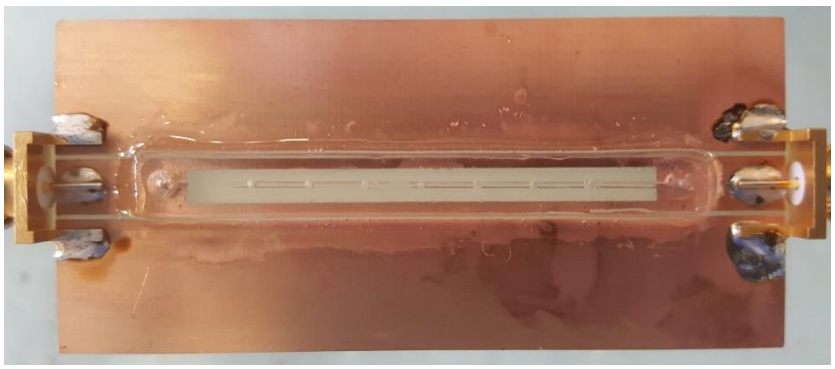

Figure 23. Fabricated H-Slot Filter with EGaIn Channel

Methodology

The frequency reconfigurability of the EGaIn H-slot filter is demonstrated by inserting two EGaIn stubs into the channel, separated by a 5mm gap. In this experiment, each stub is adjusted individually to different lengths while maintaining a constant gap between the stubs, because the total length of the slot is fixed and the objective is to examine the effect of changing the stub lengths alone without the added effects of changing the gap. Since the stub lengths are unequal, the S_{21} magnitude response of the filter will be different from the results seen in previous chapters.

There are seven holes in the middle part of the channel in addition to the two at the ends. These holes are used to inject the EGaIn stubs into one of seven test positions with greater precision. Figure 24 shows the filter with two stubs in one of the tested positions, using the holes to set the endpoints of each stub.

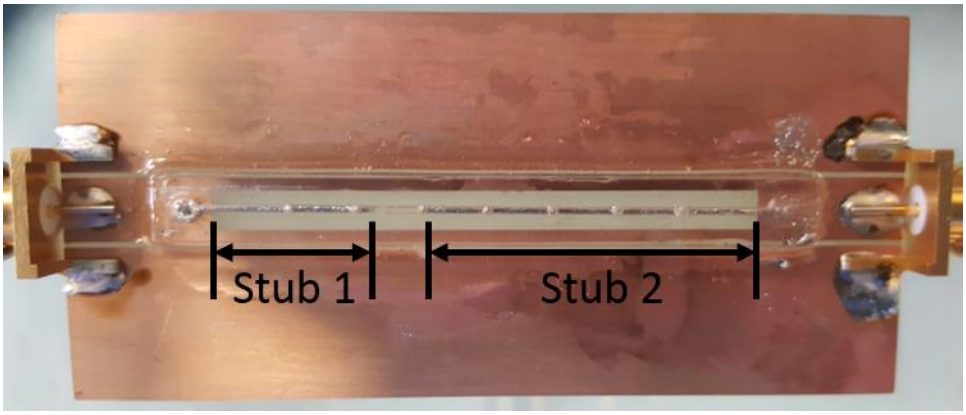

Figure 24. EGaIn H-Slot Filter Example Test Position

The first step to position the EGaIn in the channel is to cover all of the holes with tape, except for one of the holes at the end of the channel and another that marks the desired endpoint of the first stub. Then, a syringe is used to inject EGaIn into one end of the channel until it flows out of the other uncovered hole, and any excess is collected with a separate syringe. The first EGaIn stub will remain in place between the two holes, even after the tape is removed. Next, all of the holes are covered with tape again, except for the two for the endpoints of the second stub. Again, a syringe injects the EGaIn through the uncovered holes in order to position the second stub. The tape covering the other holes prevents the first stub from being disturbed by the injection of the second stub. With both stubs in place, the tape is removed and the filter is ready to be measured with a network analyzer.

There are seven stub positions tested in this experiment using the holes to set the positions as described above. Table 8 summarizes the individual stub lengths for the corresponding position number. In each of these cases, the gap between the stubs is 5 mm, which is the gap between two adjacent holes in the channel.

Position Number	Stub 1 Length	Stub 2 Length
1	6.0 mm	31.0 mm
2	11.0 mm	26.0 mm
3	16.0 mm	21.0 mm
4	18.5 mm	18.5 mm
5	21.0 mm	16.0 mm
6	26.0 mm	11.0 mm
7	31.0 mm	6.0 mm

Table 8. Stub Lengths for Corresponding Tested Positions

A slightly different procedure is used to place the stubs in position 4, since this is the equal stub length case and the holes are not directly aligned for this. In this case, the center hole and one of the holes at the end of the channel are used to set the position for each stub as previously described. However, now the flow of the EGaIn is manually stopped by releasing pressure on the syringe before the EGaIn comes out of the center hole. The endpoint for each stub is manually set to be approximately halfway between the center hole and the one adjacent to it, as shown in Figure 25.

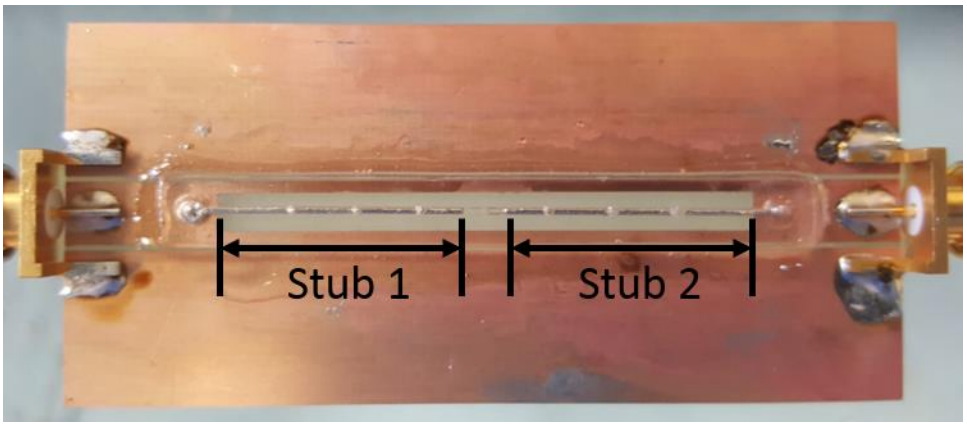

Figure 25. EGaIn H-Slot Filter in Test Position 4

Experimental Results

The measured and simulated S_{21} magnitude data for the EGaIn H-slot filter in the seven test positions of this experiment is presented in Figure 26. The results of this experiment reveal the behavior of the H-slot filter with unequal stub lengths. Figure 26 shows that there are multiple band-stop regions for the test positions with unequal stub lengths, compared to position 4, which has only one band-stop region.

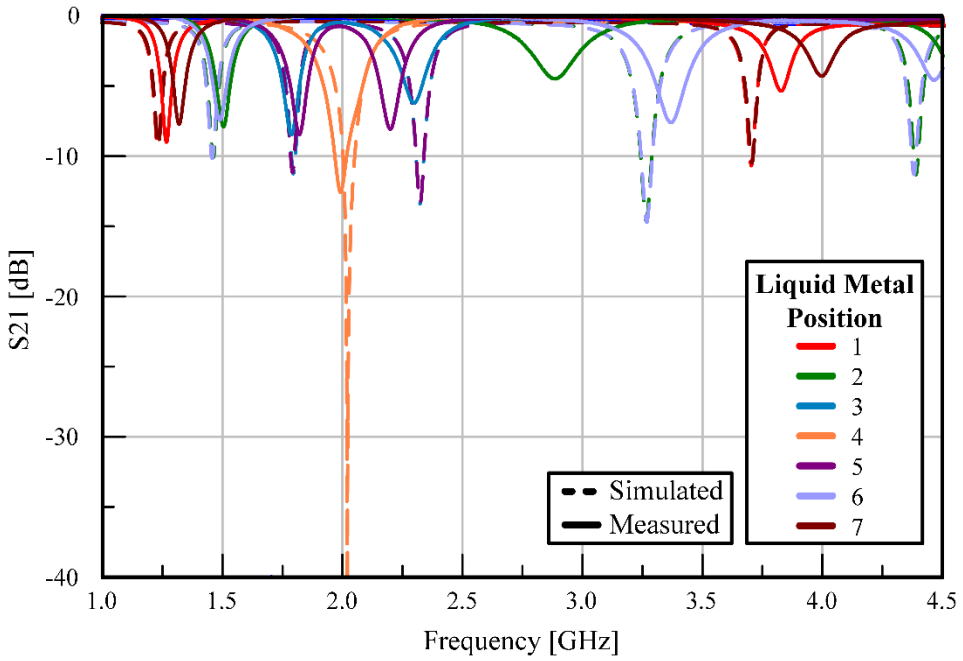

Figure 26. EGaIn H-Slot Filter Measured and Simulated S_{21} Magnitude

The reason for this is that each individual stub results in a band-stop response, with the center frequency determined by the length of the stub as noted in previous chapters. When the difference in the stub lengths is larger, such as in positions 1 and 7, the separation of the band-stop regions is greater, compared to when the stub length difference is relatively small in positions 3 and 5. As the stub length difference decreases, the band-stop regions get closer together. When the stub length difference goes to zero, as in position 4, the band-stop regions produced by each stub overlap and combine into a single region with a stronger band-stop response.

The test positions are supposed to be symmetrical with positions 1-3 being mirror images of positions 5-7 according to Table 8. The simulated data shows that this is correct, as the data for symmetric pairs of test positions completely overlap. However,

this is not the case for the measured data, which has rather large discrepancies between symmetric pairs of data, especially at the higher end of the frequency range. This is most likely due to errors in fabrication and the positioning of the EGaIn in the channel. Many of the fabrication steps were performed manually, so the actual measured device will obviously differ from the simulated model. The magnitude of S_{21} in the stop-band regions is also lower in the simulated data compared to the measured results. This is because the simulation does not account for conductor losses and other non-ideal effects that are present in a "real world" test. The measured data, however, does exhibit the general shift in band-stop regions due to the changing stub lengths. The fabricated filter could be brought into better agreement with the simulation by using more precise manufacturing techniques or by adjusting the simulation model to better reflect a "real world" test.

This experiment confirms that the fixed-length stubs of the H-slot filter can be replaced with a liquid metal to enable frequency reconfigurability. The band-stop regions of the filter can be dynamically tuned to desirable frequencies by actively controlling the position of the EGaIn stubs. The use of the acrylic channel and the EGaIn stubs in this experiment demonstrates how existing materials can be incorporated into microwave devices to enable additional functionality.

CHAPTER VI

PRINTED METAL PATCH ANTENNA

Design Overview

The printed metal patch antenna is a 2.5 GHz edge-fed microstrip patch antenna printed onto the surface of a section of stretchable spandex, using a liquid silver thermoplastic polyurethane (AgTPU) as the conductor. This antenna is developed in a cooperative effort with the Air Force Research Lab (AFRL), which fabricated the top layer of the patch antenna using a technique similar to 3D printing to deposit AgTPU on the spandex, shown in Figure 27.

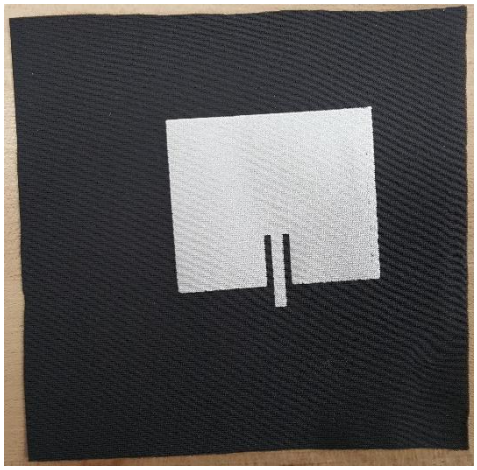

Figure 27. Top Layer of Printed Metal Patch Antenna

This device is in the early stages of development with the goal of demonstrating frequency reconfigurability of the antenna by physically stretching the supporting

spandex material. This is an example of merging traditional antenna designs with newer materials and fabrication processes to advance the capabilities of antennas in microwave systems.

The microstrip patch antenna is a well-developed antenna concept and the design process has been simplified over the years into using just a few equations to calculate the dimensions. As mentioned in Chapter 2, this design process is not the focus of this thesis and it will not be discussed in detail. A more detailed description of the design process, with all necessary equations, can be found in [6]. The printed metal patch antenna consists of the top conductor layer printed on spandex, with the spandex placed over a 31 mil RT/duroid® 5880 substrate with a dielectric constant of $\varepsilon_r = 2.2$. The spandex material is thinner than the substrate, so only the dielectric constant of the substrate is used in the design process for simplicity.

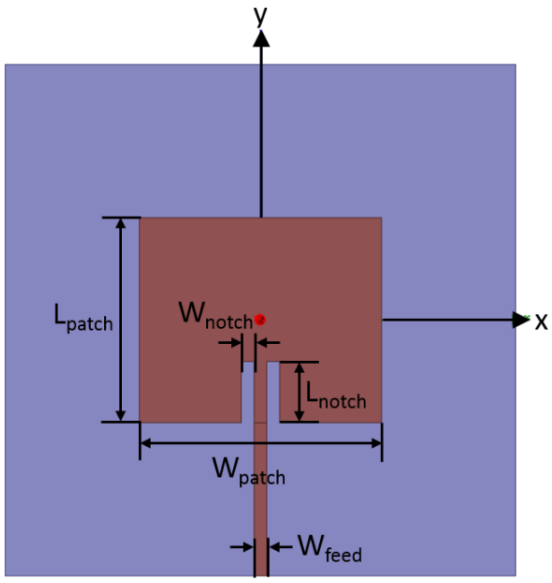

Figure 28. Diagram of Patch Antenna Design

The dimensions of the antenna, W_{patch} and L_{patch}, are calculated for an operating frequency of 2.5 GHz using the design process described in [6]. Figure 28 shows the patch antenna design modeled in HFSS with the relevant dimensions given in Table 9. The microstrip feedline width, W_{feed}, is designed for a 50 ohm transmission line. The notch width, W_{notch}, is set to be the same as the feedline width for simplicity. The notch length, L_{notch}, is found through a trial and error simulation process to impedance match the antenna as described in Chapter 2.

Dimension Name	Value
W_{patch}	47.400 mm
L_{patch}	40.107 mm
W_{feed}	2.500 mm
W_{notch}	2.500 mm
L_{notch}	12.000 mm

Table 9. Relevant Dimensions of Patch Antenna Design

The simulated VSWR and Smith chart data are shown in Figure 29 to verify that the antenna is impedance matched at the design frequency of 2.5 GHz. Antennas are considered to have an acceptable impedance match if the VSWR is below 2. Figure 29 shows that the VSWR is approximately 1 at 2.5 GHz, which corresponds to where the blue trace on the Smith chart touches the center, so this antenna is considered impedance matched at 2.5 GHz.

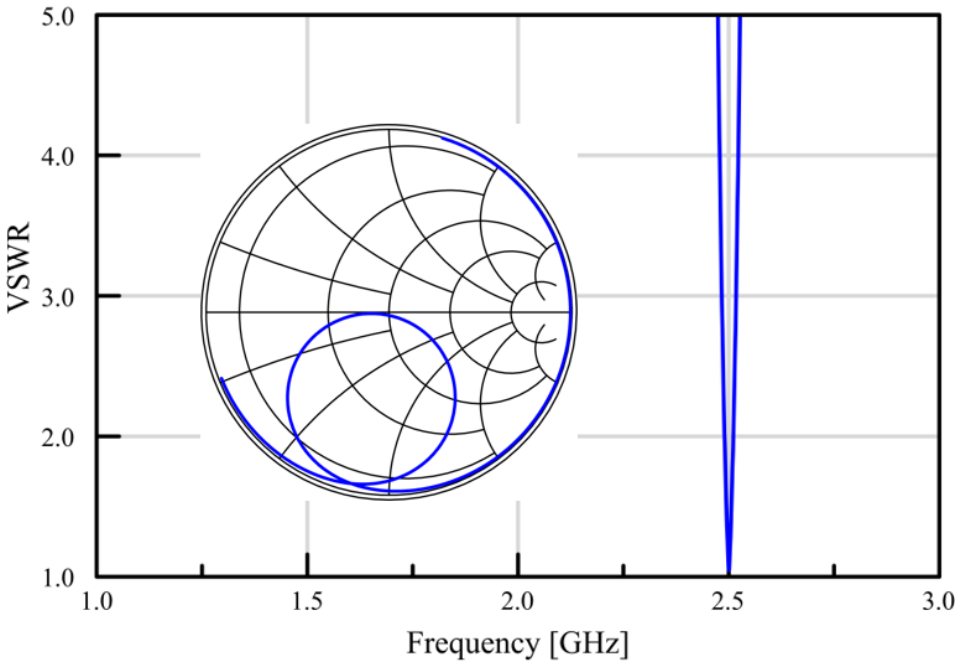

Figure 29. Simulated VSWR and Smith Chart for Patch Antenna Design

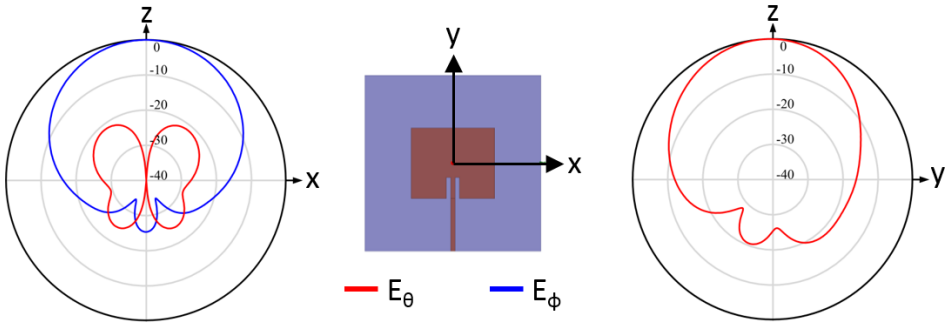

Figure 30. Normalized Radiation Patterns of Patch Antenna Design

Figure 30 shows the normalized radiation patterns for the xz-plane and yz-plane, which are the H-plane and E-plane for this antenna, respectively. The shape of the radiation patterns in Figure 30 show that this antenna radiates like a typical patch

antenna, with the peak gain in the positive-z direction and the electric field linearly polarized in the y-direction.

This antenna design follows a standard design process and results in the typical VSWR and radiation pattern data for a patch antenna. The more interesting thing about this experiment is the materials on which the antenna is fabricated. With the antenna model verified to operate like a standard patch antenna in simulation, the design is sent to the AFRL for fabrication using AgTPU as the conductor on a piece of spandex material.

Experimental Results

The spandex piece with the printed patch design that is received from the AFRL needs to be attached to a feed line on the RT/duroid® 5880 substrate, which includes the ground plane, in order to create a functioning patch antenna. The microstrip feedline for this antenna is a strip of copper tape placed on the substrate that is lifted up at the end to join with the printed AgTPU feedline section on the spandex. Copper tape was chosen to make the feedline because it can make the transition from the substrate to the spandex and connect to the printed patch. Additional AgTPU, supplied by the AFRL, is applied to the feedline junction to help the copper tape feedline make good electrical contact with the printed patch, as shown in Figure 31. The AgTPU texture is similar to acrylic paint, and it can be brushed onto the junction with a small paintbrush.

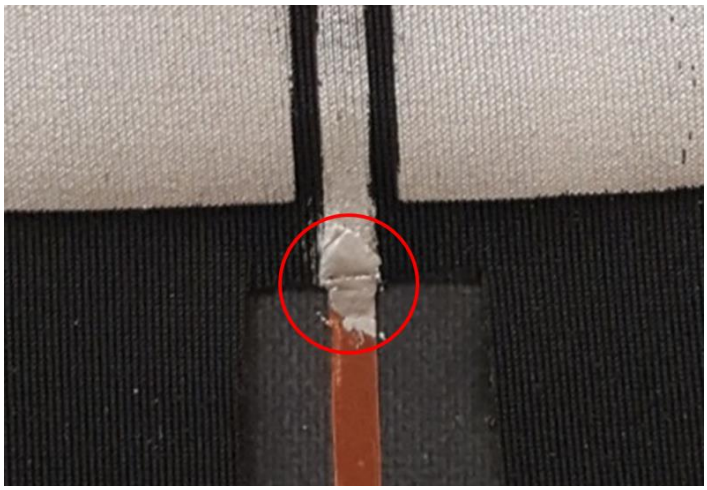

Figure 31. Feedline Junction of Fabricated Printed Metal Patch Antenna

With the spandex piece in place, the antenna is clamped between two pieces of foam, as shown in Figure 32, in order to keep the spandex flat against the substrate and prevent it from moving and breaking the connection with the feedline.

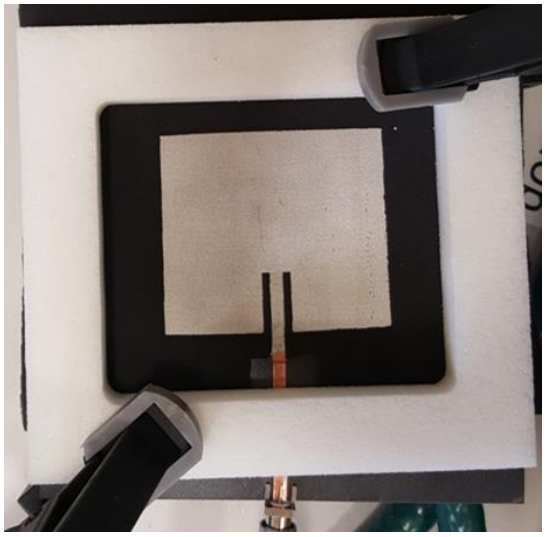

Figure 32. Printed Metal Patch Antenna with Foam Cover for Support

The foam has a dielectric constant similar to air so that it has a minimal effect on the antenna performance. Better methods for assembling and feeding this antenna could be developed, but this is just a prototype to show that an antenna can be made using the printed AgTPU.

The measured VSWR and Smith chart of the assembled antenna are shown in Figure 33(a) with the antenna feed point indicated in Figure 33(b). The antenna has a poor impedance match with a VSWR above 3, and the operating frequency of the fabricated antenna is slightly higher than what the simulation predicts. The poor impedance match can be attributed to effects from the copper-tape-to-AgTPU junction and other effects not captured in the simulation. It is not necessary to have the antenna operate precisely at 2.5 GHz for now, since it is still in the prototype stage and this issue can be fixed by adjusting the length of the patch in the future designs.

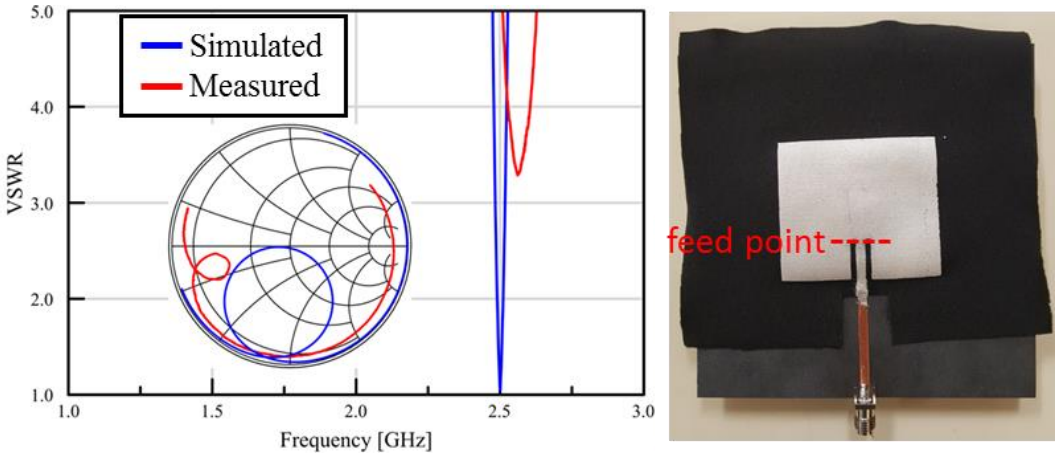

(a) (b)

Figure 33. Original Printed Metal Patch Antenna (a) VSWR and Smith Chart and (b) Feed Point Location

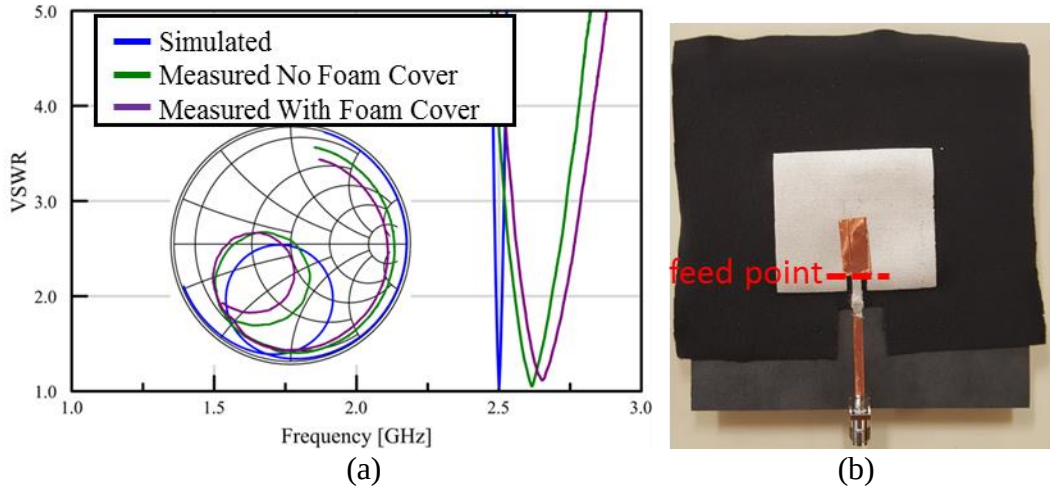

(a) (b)

Figure 34. Printed Metal Patch Antenna Impedance Matched with Copper Tape (a) VSWR and Smith Chart and (b) Feed Point Location

Fortunately, patch antennas can be easily impedance matched by adjusting the feed point where the transmission line meets the patch, as described in Chapter 2. A piece of copper tape is used to provide a temporary impedance match and prove that the method works. Figure 34(a) shows the VSWR and Smith chart of the fabricated antenna with a piece of copper tape used to shift the feed point closer to the edge of the patch, shown in Figure 34(b). The antenna is measured with and without the foam cover piece clamped to the antenna in order to show how holding the spandex flat against the substrate affects the performance. The copper tape piece provides a good impedance match for the antenna at a frequency around 2.65 GHz, with a measured minimum VSWR very close to 1 with and without the foam cover. The foam cover has little effect on the performance in this case.

With the copper tape method proving to solve the impedance match issue, a more permanent solution, using the extra AgTPU provided by the AFRL, is tested. The

AgTPU is brushed on to the patch antenna to shift the feed point closer to the edge of the patch. The antenna VSWR is continuously monitored during this process in order to signal when to stop shifting the feed point, because the AgTPU is very difficult to remove and there is a risk of overshooting the correct feed point.

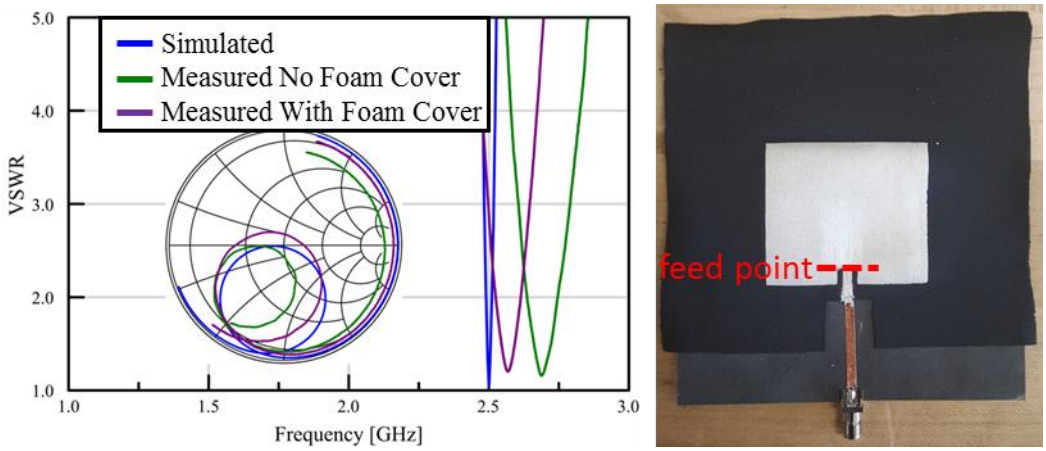

(a) (b)

Figure 35. Printed Metal Patch Antenna Impedance Matched with AgTPU (a) VSWR and Smith Chart and (b) Feed Point Location

Figure 35(a) shows the measured VSWR and Smith chart of the antenna with the AgTPU used to shift the feed point closer to the edge of the patch, shown in Figure 35(b). The AgTPU method results in a VSWR close to 1 at about 2.69 GHz without the foam cover. The VSWR minimum shifts to about 2.57 GHz when the foam cover is clamped to the antenna. This measurement shows that the AgTPU can be used to impedance match the antenna, though not at the desired frequency of 2.5 GHz. As previously stated, the center frequency difference is a minor issue that could be solved by adjusting the length of the patch in future designs.

While the antenna was impedance matched using the copper tape, the radiation pattern of the antenna was measured in an anechoic chamber. The measured radiation pattern of the antenna with the copper tape impedance matching is shown in Figure 36(a), normalized to the measured peak gain of this antenna. The radiation pattern of the antenna was measured again after the antenna was permanently impedance matched using the AgTPU. Figure 36(b) shows the measured radiation pattern of the antenna with the AgTPU impedance matching, again normalized to the measured peak gain. The normalized radiation patterns for the simulated antenna are shown in Figure 36(c) for comparison.

Recall that there are differences in the operating frequencies of the different measured antenna configurations. The radiation patterns in Figure 36 are measured at the respective operating frequencies of each antenna configuration in order to display the best radiation performance for each antenna. The focus of these measurements is to compare the general shape of the fabricated and simulated antenna radiation patterns in order to verify that the fabricated antenna behaves like a typical patch antenna.

Figure 36 shows that both the copper tape matched and the AgTPU matched antennas have similar radiation patterns compared to the simulation. Both fabricated antenna configurations are linearly polarized in the y-direction, however, the copper tape matched antenna exhibits a stronger cross-polarization than the AgTPU matched antenna. The AgTPU matched antenna has a larger back lobe in the xz-plane (H-plane) compared to the copper tape matched antenna and the simulated antenna.

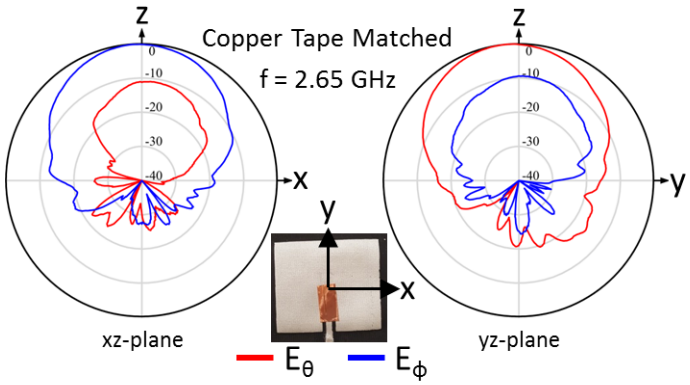

(a)

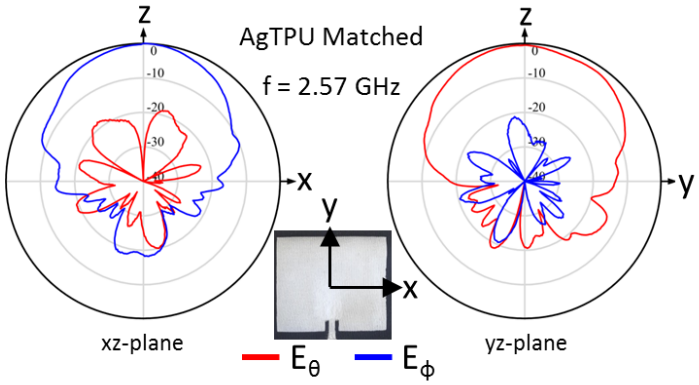

(b)

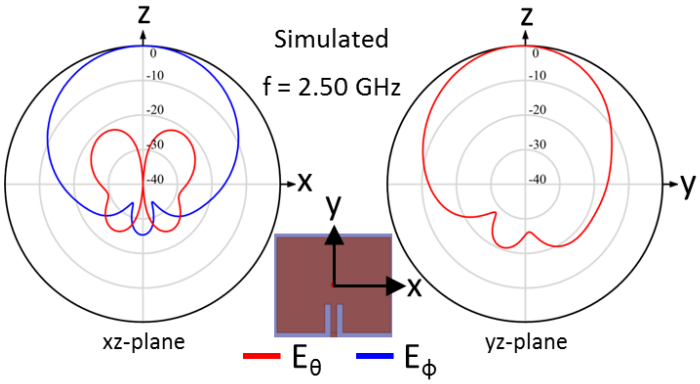

(c)

Figure 36. Normalized Radiation Patterns of Printed Metal Patch Antenna (a) with Copper Tape Impedance Matching (b) with AgTPU Impedance Matching and (c) Simulated

The data presented in this section confirms that, after some minor adjustments, the patch antenna fabricated using AgTPU on spandex behaves like a typical patch antenna. The data collected in this study will be used to guide the development of future iterations of this design.

Simulated Stretching Reconfigurability

The printed metal patch antenna is designed with the goal of enabling frequency reconfigurability by physically stretching the length of the patch. Recall from Chapter 2 that the length of the patch is designed to be approximately a half-wavelength at the fundamental operating frequency; thus, changing the length will affect the operating frequency. The impedance and radiation performance of the un-stretched fabricated patch antenna is verified through the measurements in the previous section. The current assembly of the printed metal patch antenna does not allow for controlled stretching, so simulations are used to demonstrate how stretching the antenna affects its operating frequency. Two different types of stretching are presented in this section, and the results of the simulations will be used to aid in developing an apparatus for controlling the stretching of the fabricated antenna.

The first type of stretching presented will be referred to as "proportional stretching". This is conceptually the simplest form of stretching, where both the length of the patch and the length of the notch for the feed point are multiplied by the same factor. Figure 37 shows an example of proportional stretching, in which the length of the patch, L_{patch}, and the length of the notch, L_{notch}, are both stretched by a factor of 1.5.

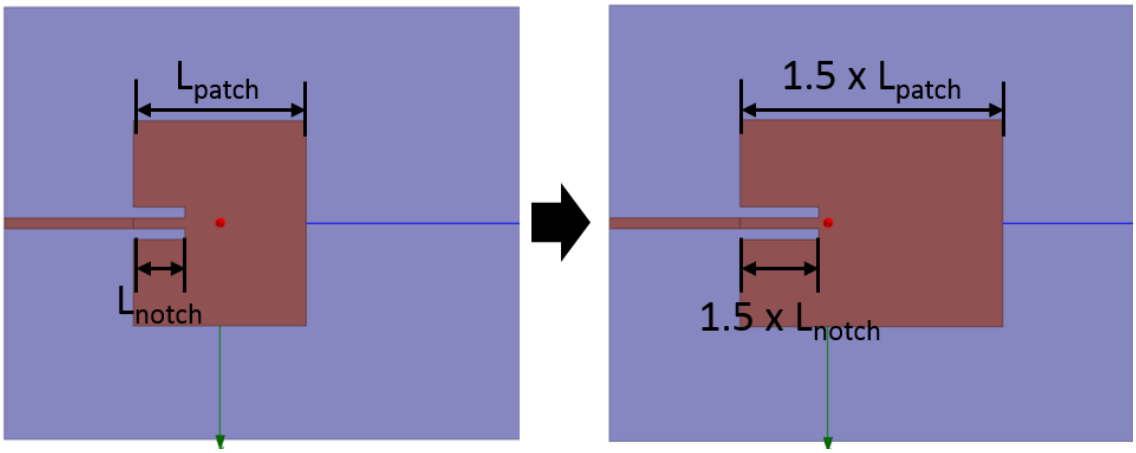

Figure 37. Diagram of Proportional Stretching Method (Stretch Factor = 1.5)

Simulations of proportional stretching are conducted for stretch factors between 1.0 and 1.5. Table 10 shows the values of L_{patch} and L_{notch} used in this simulation with the corresponding proportional stretch factors.

Proportional Stretch Factor	L_{patch}	L_{notch}
1.0	40.107 mm	12.000 mm
1.1	44.118 mm	13.200 mm
1.2	48.128 mm	14.400 mm
1.3	52.139 mm	15.600 mm
1.4	56.150 mm	16.800 mm
1.5	60.161 mm	18.000 mm

Table 10. Relevant Dimensions of Patch Antenna and Corresponding Proportional Stretch Factors

The VSWR data for the proportional stretching simulation is shown in Figure 38. The operating frequency of the antenna, indicated by the minimum VSWR point, decreases as the patch length increases.

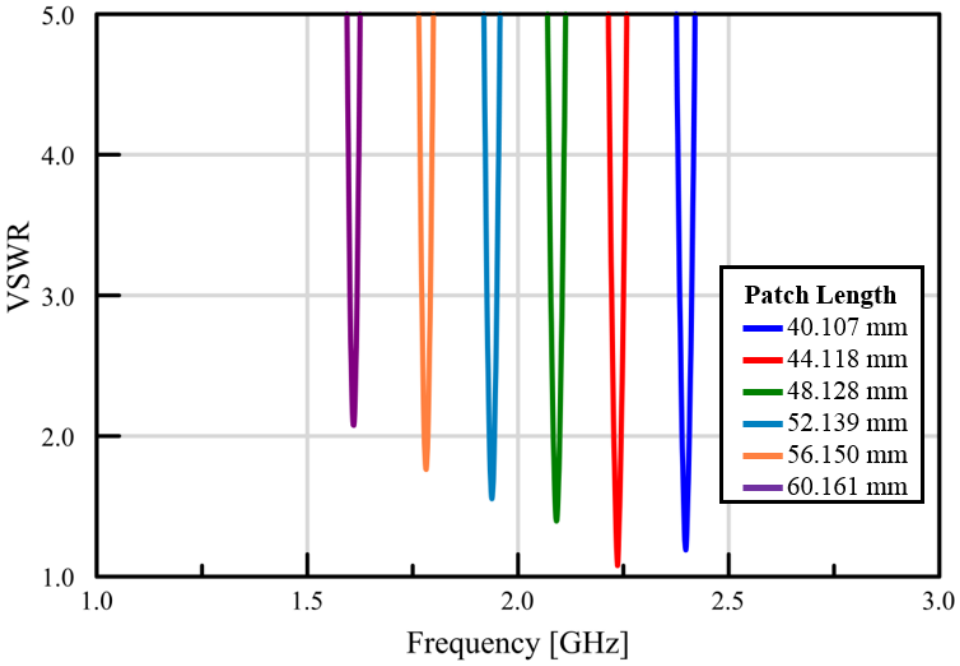

Figure 38. Patch Antenna VSWR for Proportional Stretching Simulation

This demonstrates that the antenna is made frequency reconfigurable through the proportional stretching of the patch. The VSWR data indicates that the impedance match worsens as the patch length is increased beyond 44.118 mm. The antenna has a poor impedance match, indicated by a minimum VSWR above 2, when stretched to a patch length of 60.161 mm, limiting the tunable frequency range of the antenna.

The Smith chart data in Figure 39 provides more information about the impedance match of the antenna for the different simulated proportional stretch factors. As the stretch factor increases, the corresponding circular curve on the Smith chart enlarges. Recall from Chapter 2 that such a shift in the Smith chart curve indicates that the input impedance is increasing as the stretch factor increases. The impedance mismatch that occurs as the stretch factor increases can be corrected by increasing the

notch length to move the feed point closer to the center of the patch in each stretch position.

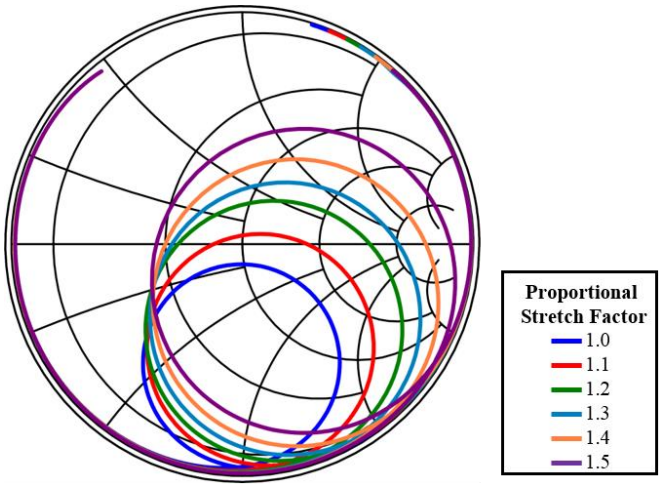

Figure 39. Patch Antenna Smith Chart for Proportional Stretching Simulation

The second type of stretching presented involves proportionally stretching only the half of the patch that contains the notches that create the feed point, as shown in Figure 40. This form of stretching will be referred to as “half-proportional stretching”.

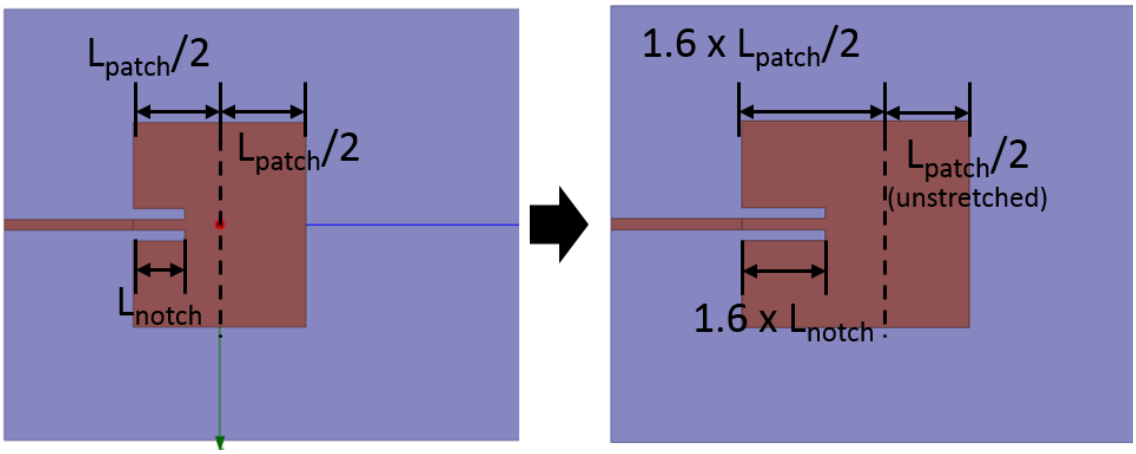

Figure 40. Diagram of Half-Proportional Stretching Method (Stretch Factor = 1.6)

Simulations of half-proportional stretching are conducted for stretch factors that result in the same patch lengths used in the proportional stretching simulations, in order to allow for a more direct comparison between the two stretching methods. The only difference in this simulation compared to the previous one is that the notch lengths in this simulation are greater for each corresponding patch length. Table 11 shows the values of L_{patch} and L_{notch} used in this simulation with the corresponding half-proportional stretch factors.

Half-Proportional Stretch Factor	L_{patch}	L_{notch}
1.0	40.107 mm	12.000 mm
1.2	44.118 mm	14.400 mm
1.4	48.128 mm	16.800 mm
1.6	52.139 mm	19.200 mm
1.8	56.150 mm	21.600 mm
2.0	60.161 mm	24.000 mm

Table 11. Relevant Dimensions of Patch Antenna and Corresponding Half-Proportional Stretch Factor

The VSWR data for the half-proportional stretching simulation in Figure 41 shows that the antenna maintains an acceptable impedance match, indicated by a minimum VSWR below 2, as the antenna is stretched to 60.161 mm. This shows that using half-proportional stretching extends the tunable frequency range beyond that of the proportionally stretched antenna.

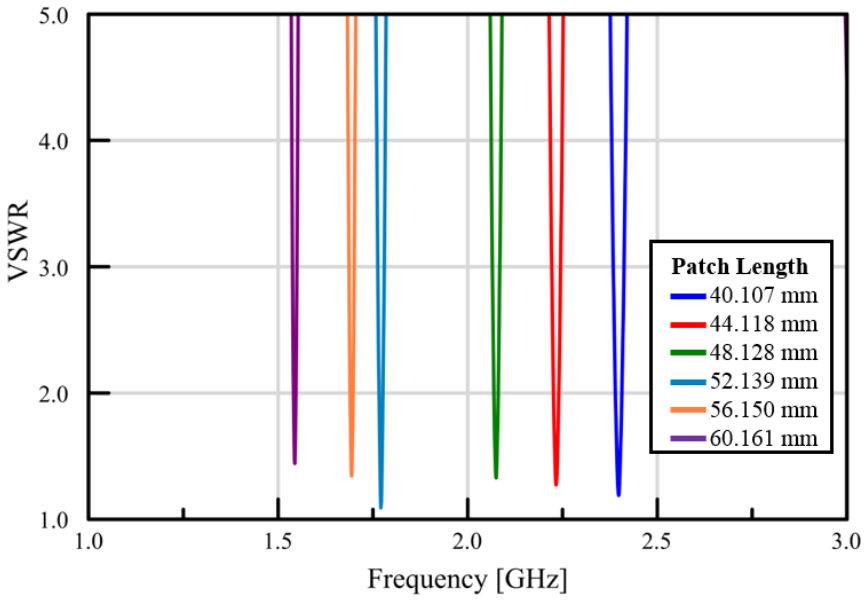

Figure 41. Patch Antenna VSWR for Half-Proportional Stretching Simulation

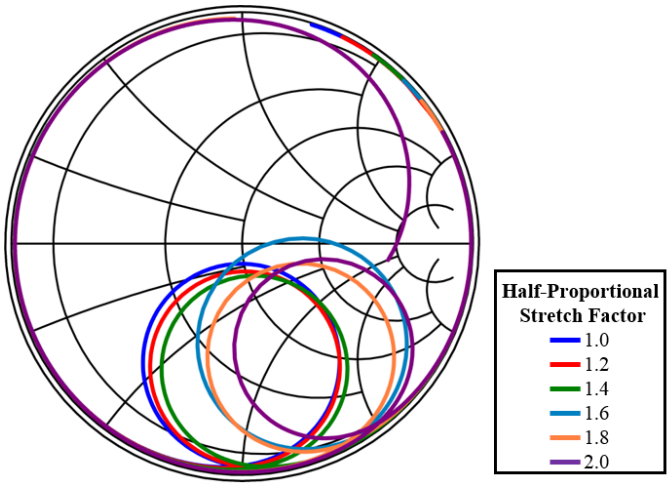

Figure 42. Patch Antenna Smith Chart for Half-Proportional Stretching Simulation

Figure 42 shows the Smith chart curves of the antenna for the different half-proportional stretch factors. Each curve resembles that of a well-matched patch antenna,

and the input impedance does not increase significantly with the stretch factor as it did with proportional stretching.

Both stretching methods presented in this section demonstrate the ability to shift the center frequency of the patch antenna. However, the half-proportional stretching method is shown to have the advantage of enabling a wider tunable frequency range for the antenna. The information gathered from these simulations will aid in the design of a stretching apparatus that optimizes the frequency reconfigurability of the printed metal patch antenna as the development of this project continues.

CHAPTER VII

MICROSTRIP PATCH ANTENNA WITH INTEGRATED PUMPING MECHANISM

Design Overview

The fluid reconfigurable filter discussed in Chapter 4 uses an external pumping system to push fluid through a channel to reconfigure the device. This chapter discusses the development of a prototype microstrip patch antenna with an integrated pumping mechanism, named “Pumptenna”, which explores the concept of incorporating the pump system for a fluid reconfigurable device into the design of the device itself. The pumping mechanism in this design is intended to be only a means of moving the fluid in a reconfigurable system, and thus it does not make the device reconfigurable by itself. In fact, the goal of the pumping mechanism is to move fluid through a channel in a way that minimizes the effect on the behavior of the patch antenna. This allows the pumping mechanism to be used in a variety of reconfigurable systems in which any inherent effects of the pump may counteract the intended operation of the system. The development of the Pumptenna prototype is enabled by 3D-printed structures and other materials finding new uses in the design of reconfigurable antennas.

The Pumptenna consists of a microstrip patch antenna supported by a 3D-printed platform over a ground plane. The 3D-printed platform includes a fluid channel, 1.5 mm in diameter, between the ground plane and top layer of the patch antenna with a cylindrical reservoir in the center. The top layer of the patch has a circular section cut out for the reservoir and a thin, flexible, non-conductive material covers the reservoir

like a bubble instead. Figure 43 shows the diagrams of the top view and side view of the Pumptenna model in HFSS. The relevant dimensions of this design are summarized in Table 12.

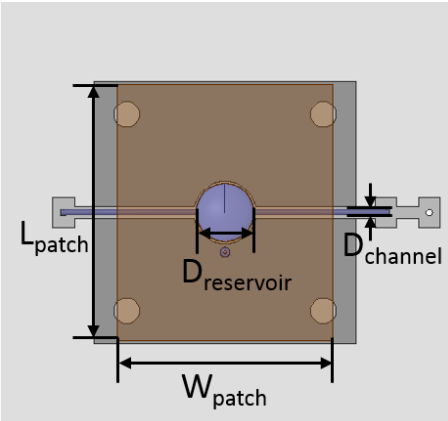

(a)

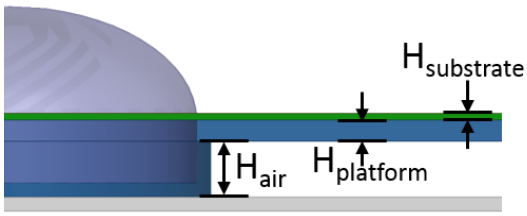

(b)

Figure 43. Diagram of Pumptenna (a) Top View (b) Side View

Dimension Name	Value
L_{patch}	119.0 mm
W_{patch}	100.0 mm
$D_{reservoir}$	27.0 mm
$D_{channel}$	1.5 mm
H_{air}	4.0 mm
$H_{platform}$	1.5 mm
$H_{substrate}$	20 mil

Table 12. Relevant Dimensions of Pumptenna

The dimensions of the top patch layer follow the standard patch antenna design process discussed in [6]. The patch antenna is designed for a center frequency of 1 GHz so that the features in the 3D-printed platform are large enough for the resolution of the printer. The top layer of the patch antenna is copper on a 20 mil RT/duroid® 5880 substrate.

The pumping mechanism is formed by placing a one-way check valve on each side of the fluid channel such that fluid flows in one direction. Figure 44 illustrates the action of the pumping mechanism.

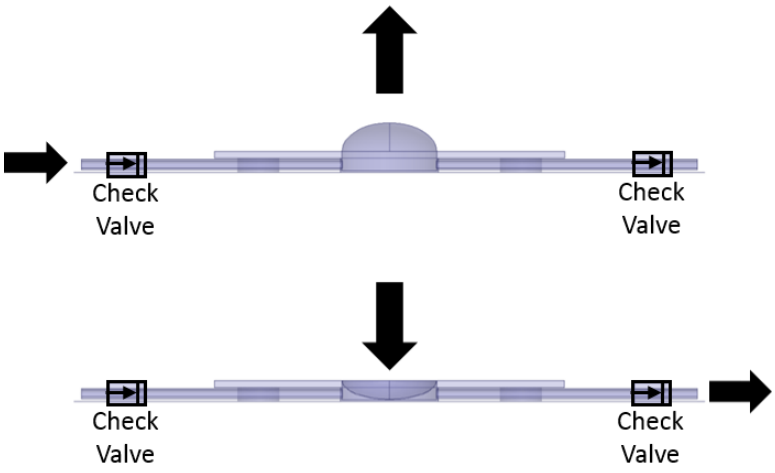

Figure 44. Pumping Mechanism Action

The flexible material that covers the reservoir can move up and down to change the volume of the reservoir. As the flexible cover expands upward, it draws fluid into the reservoir through the check valve on one end of the channel. When the flexible cover is pushed down, it forces the fluid out of the reservoir through the check valve on the other

end of the channel. This flexing cycle repeats to pump fluid through the channel, which can be connected to a larger fluid network that enables reconfigurability of the antenna or other nearby devices.

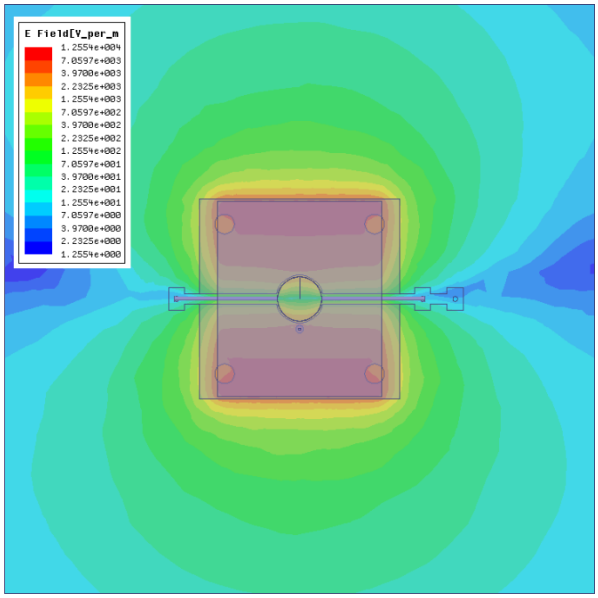

Figure 45. Electric Field Magnitude of Pumptenna (XY-Plane)

Figure 45 shows the electric field magnitude in the xy-plane between the top patch layer and the ground plane. The fluid channel and reservoir that form the pump mechanism are placed along the electric field minimum through the center of the antenna in order to minimize the effects that the fluid may have on the behavior of the antenna. From there, the fluid channel could be routed to different regions of the antenna to enable reconfigurability, but the pump itself should maintain a minimal impact on the antenna's performance.

HFSS Simulation

The Pumptenna is simulated in HFSS to examine the impedance and radiation characteristics of the antenna. The simulation is intended to illustrate specifically how the antenna characteristics change throughout the pumping cycle, therefore the simulation is conducted with the flexible reservoir cover at its minimum, flat, and maximum positions in the cycle. The simulation is also conducted with fluid dielectric constants of $\varepsilon_r = 2$ and $\varepsilon_r = 16$ to illustrate the differences when using a relatively low dielectric constant fluid compared to a higher dielectric constant.

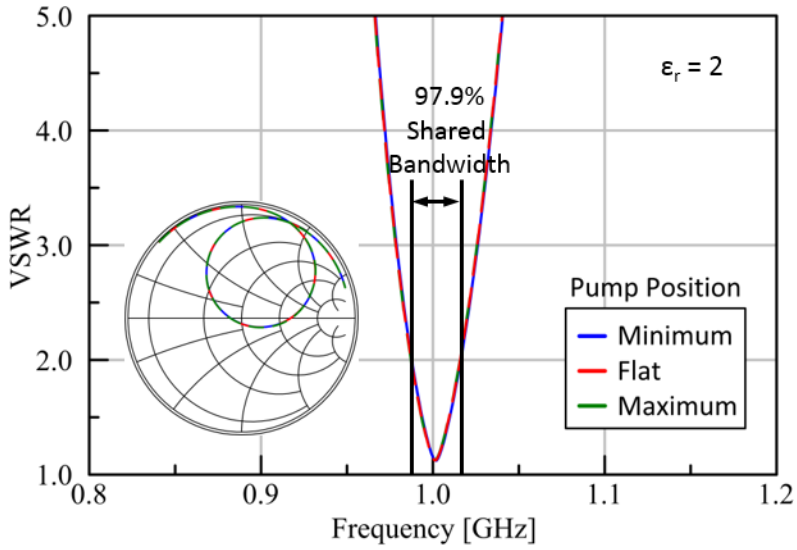

Figure 46. VSWR of Pumptenna for Different Pump Positions ($\varepsilon_r = 2$)

Figure 46 shows the VSWR and Smith chart of the antenna for the different pump positions using a fluid dielectric constant of $\varepsilon_r = 2$. The bandwidth of an antenna is the width of the frequency range for which the VSWR is below 2, indicating an

acceptable impedance match. For this simulation, the important characteristic is what will be referred to as the shared bandwidth, or the width of the frequency range for which the VSWR is below 2 for *all* pump positions. The shared bandwidth is expressed as a percent of the bandwidth of the antenna when the pump is in the flat position. The shared bandwidth for the antenna using a fluid dielectric constant of $\varepsilon_r = 2$ is 97.9% of the flat position bandwidth. This means that the antenna bandwidth is not affected much by the pumping mechanism, which is a goal of this design.

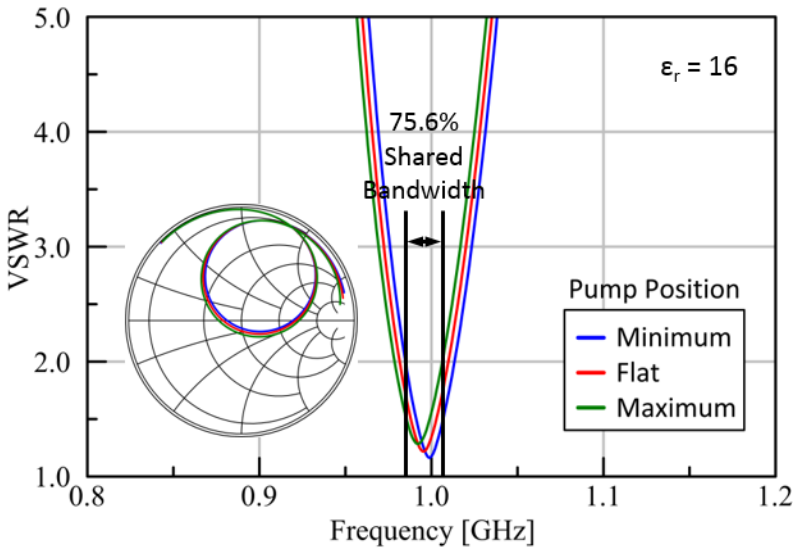

Figure 47. VSWR of Pumptenna for Different Pump Positions ($\varepsilon_r = 16$)

Figure 47 shows the VSWR and Smith chart of the antenna for the different pump positions using a fluid dielectric constant of $\varepsilon_r = 16$. In this case, the VSWR curve shifts more between the different pumping positions and the shared bandwidth is only 75.6% of the flat position bandwidth. This shows that the pumping mechanism has a

greater impact on the impedance bandwidth of the antenna when the fluid dielectric constant is greater. However, the pump does not have a significant impact on the antenna bandwidth for relatively low fluid dielectric constants.

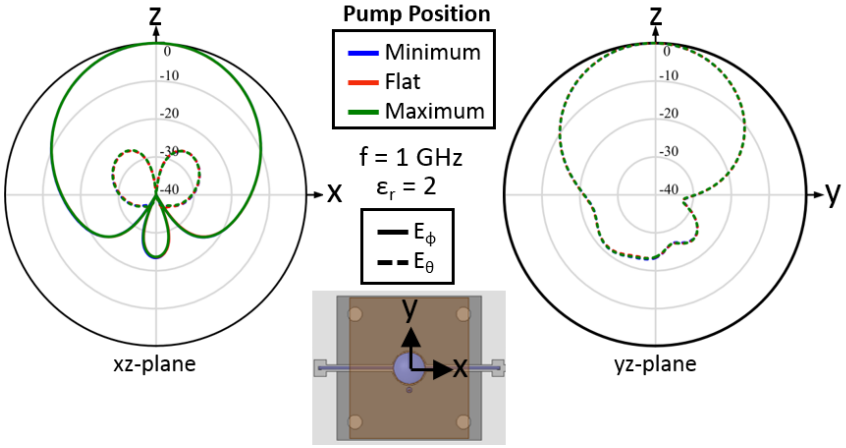

Figure 48. Normalized Radiation Patterns of Pumptenna for Different Pump Positions ($\varepsilon_r = 2$)

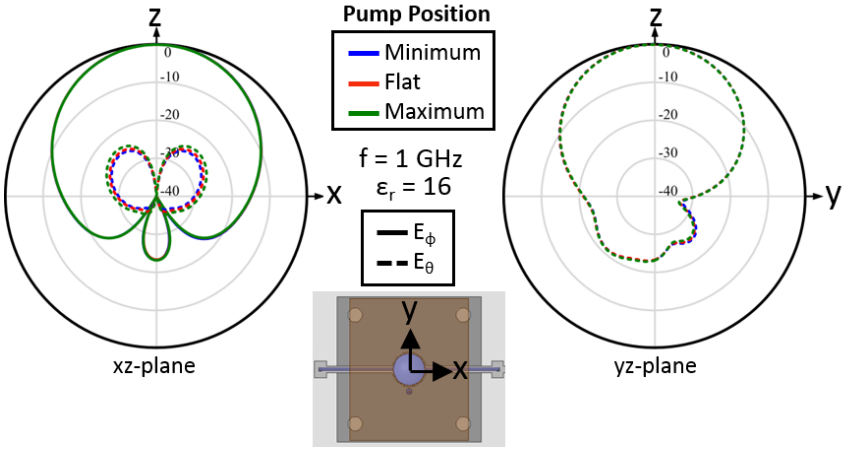

Figure 49. Normalized Radiation Patterns of Pumptenna for Different Pump Positions ($\varepsilon_r = 16$)

Figure 48 shows the normalized radiation patterns for the Pumptenna in the xz-plane and yz-plane for each pump position using a fluid dielectric constant of $\varepsilon_r = 2$. There is no noticeable change in the radiation pattern as the pump cycles through the different positions. Figure 49 shows the normalized radiation patterns for the Pumptenna in the xz-plane and yz-plane for each pump position using a fluid dielectric constant of $\varepsilon_r = 16$. The only noticeable difference between the different pump positions is that the cross-polarization (E_θ) gain increases slightly as the pump goes from the minimum to maximum position. This is not a significant change in the radiation pattern, so the pumping mechanism does not have a significant impact on the radiation performance of the antenna for either fluid dielectric constant.

The simulation of the Pumptenna indicates that the pumping mechanism can have a significant effect on the antenna bandwidth if the fluid dielectric constant is relatively high. However, the pump does not have a significant impact on the radiation characteristics of the antenna, even with a relatively high fluid dielectric constant. These results show that this design achieves the goal of integrating a pumping mechanism into the antenna structure without significantly affecting the performance of the antenna.

Prototype Development

A prototype of the Pumptenna is currently being developed to demonstrate the operation of the pumping mechanism and to confirm the simulated results. The prototype, shown in Figure 50, uses 3D-printed polylactic acid (PLA) to create the platform with the fluid channel and reservoir. The flexible reservoir cover is a piece of

latex rubber stretched over the reservoir and sealed with epoxy. This piece of latex is covered by a 3D-printed hemispherical cap connected to a pneumatic line to control the flexing of the pump.

Figure 50. Pumptenna Prototype

The challenges in developing this prototype involve sealing the fluid channel and the reservoir cover piece. The 3D-printed platform is being redesigned to create better surfaces for applying the sealant. Though it is not yet complete, this prototype is another example of the efforts to utilize new materials and manufacturing techniques to enable reconfigurable antennas.

CHAPTER VIII

CONCLUSIONS

The first H-slot filter presented in this thesis demonstrated the use of a 3D-printed fluid channel to enable frequency reconfigurability. The techniques discussed for designing and sealing the fluid channel are transferrable to other similar designs, facilitating the process for designing and fabricating future reconfigurable devices. The method for developing an expression to determine the dielectric constant of the fluid in the filter from the frequency response of the filter can be extended to other devices. This could allow other microwave devices to be used as sensors for material characterization applications.

The H-slot filter with the EGaIn stubs is an example of how liquid conductors can be used to create physically reconfigurable microwave devices. The use of the extra holes in the acrylic channel demonstrates a method for accurately positioning the EGaIn, which is a challenge in designs that use such liquid metals. The results of the asymmetrical stub experiment revealed that there are individual stop-band regions in the frequency response corresponding to the length of each stub. This insight can be used in the future development of series-stub CPW filters.

The development of the printed metal patch antenna prototype demonstrates a fabrication technique of printing a liquid conductor, AgTPU, on a stretchable fabric. AgTPU was used to improve the electrical connection between the copper tape feedline and the AgTPU patch. AgTPU was also used to impedance match the antenna by

adjusting the feed point location. The steps for assembling the printed metal patch antenna prototype serve as a guide for the development of future devices using AgTPU on spandex. The stretching simulations show how this antenna can be made frequency reconfigurable. The simulations revealed that the half-proportional stretching method results in a better impedance match throughout the stretching process compared to proportional stretching. A mechanism for enabling half-proportional stretching in the prototype will be developed to verify these results experimentally as part of the ongoing work for this project.

The concept of the patch antenna with an integrated pumping mechanism, or "Pumptenna", is an example of incorporating flexible materials in reconfigurable antenna systems. The pumping action is enabled by a flexible latex material in the center of the patch antenna. Simulations show that the effects of the pumping action on the antenna performance become more noticeable as the dielectric constant of the fluid in the channel increases. A prototype is being developed as part of the ongoing work for this project in order to verify the simulated results and to address the challenges involved in incorporating the flexible latex material with the 3D-printed fluid structure for the antenna.

The devices presented in this thesis serve as demonstration vehicles to address the challenges in fabricating and measuring reconfigurable microwave devices using new materials. The design, fabrication, and measurement procedures for each device were discussed to provide a guide for future collaboration between the material science and microwave engineering communities.

REFERENCES

[1] A. Dey, A. Kiourti, G. Mumcu, and J. L. Volakis, "Microfluidically Reconfigured Frequency Tunable Dipole Antenna," in *2015 9th European Conference on Antennas and Propagation (EuCAP)*, 2015, pp. 1-2.

[2] D. Dubuc and K. Grenier, "Microfluidic-Based Tunable RF True-Time Delay Line," in *Microwave Conference (EuMC), 2010 European*, 2010, pp. 1222-1224.

[3] W. Su, R. Bahr, S. A. Nauroze, and M. M. Tentzeris, "3D Printed Reconfigurable Helical Antenna Based on Microfluidics and Liquid Metal Alloy," in *2016 IEEE International Symposium on Antennas and Propagation (APSURSI)*, 2016, pp. 469-470.

[4] M. Konca and P. A. Warr, "A Frequency-Reconfigurable Antenna Architecture Using Dielectric Fluids," *IEEE Transactions on Antennas and Propagation*, vol. 63, pp. 5280-5286, 2015.

[5] R. E. Collin, *Foundations for Microwave Engineering*, 2 ed. Hoboken, NJ: Wiley, 2001.

[6] C. A. Balanis, *Antenna Theory: Analysis and Design*, 3 ed. Hoboken, NJ: John Wiley & Sons, 2005.

[7] D. M. Pozar, *Microwave Engineering*, 4 ed.: Wiley, 2012.

[8] K. Chang, *Microwave Solid-State Circuits and Applications*: Wiley, 1994.

[9] A. Ghosh and R. V. R. Choudhury, "Design and Fabrication of a S Band Multi-Stub CPW Band Pass Filter for Improved Filter Characteristics," in *2015 International Conference on Microwave and Photonics (ICMAP)*, 2015, pp. 1-2.

[10] G. E. Ponchak and L. P. B. Katehi, "Open- and Short-Circuit Terminated Series Stubs in Finite-Width Coplanar Waveguide on Silicon," *IEEE Transactions on Microwave Theory and Techniques,* vol. 45, pp. 970-976, 1997.

[11] S. van de Geer, "Least Squares Estimators," in *Encyclopedia of Statistics in Behavioral Science* vol. 2, B. S. Everitt and D. C. Howell, Eds., ed. Chichester: Wiley VCH, 2005, pp. 1041-1045.